Development and Evaluation of a Sensor and Antenna Array for a Portable Microwave-Based Breast Cancer Detection System

by

Muhammad Masud Rana

A Thesis submitted to the Faculty of Graduate Studies of
The University of Manitoba
in partial fulfillment of the requirements of the degree of

MASTER OF SCIENCE

Biomedical Engineering
University of Manitoba
Winnipeg, Manitoba, Canada

ABSTRACT

Breast microwave sensing (BMS) is a novel breast screening technique for detecting breast cancer based on detecting the dielectric contrast between cancer and breast healthy tissue. The current BMS systems are designed for use in clinical environments and are not suited for use in remote locations due to the hardware setup.

This dissertation describes research conducted as part of developing a prototype portable breast microwave sensing (BMS) system for early breast cancer detection. The portable BMS system includes a scanning chamber, transmitter and receiver sensors on a semi-circular platform and the data measurement software used to control it. The portable system uses a horn antenna to transmit frequencies from 1.5 GHz to 6 GHz. A single receiver antenna was characterized at different distances from the transmitter. The symmetry of the semicircular receiver platform was investigated with respect to a reference antenna directly in line with the beam axis of the horn antenna, and with a 20 cm spacing. Another receiver antenna was placed at 0 cm and 1 cm horizontal separation from the reference antenna's immediate to its left or right side. This thesis investigated the response of the antenna sensor array to a point scatterer, using simulation and experiment. This study compares the E-field characteristics and DC voltages for each sensor, using simulation in CST Microwave Studio version 2019 and experimental results for both a free air system and with an Aluminum rod placed at 83 positions in the scanning plane.

From the symmetrical analysis, the percentage of differences in the signal strength between the antenna placed to the left or right side of the reference antenna in the receiver were determined to be $(0.22 \pm 1.63)\%$ and $(-0.17 \pm 1.74)\%$ respectively, for 0 cm and 1 cm distance from the reference antenna. Each antenna element experienced mutual coupling with the antenna's on its immediate left and right in the receiver array. The optimal separation of each antenna in the receiver array was calculated to be 4 mm based on an envelope correlation coefficient of 0.37. The semi-circular receiver sensor array was built using thirteen patch antennas with a 4 mm separation between antennas.

The portable BMS system was calibrated using a 13×10 array of geometric correction constants, which were calculated from the simulated E-field. The differences between the simulated and experimental results ranged from -4% to 3% for open space conditions and $\pm 15\%$ when an Aluminum rod was placed at different positions in the scanning plane. The receiver

antenna array's measured power ranged from 10.3 dBm to 9.3 dBm at a 95% CI under open space conditions. The maximum value of the average relative power (ARP) was 1.63, and the minimum value of the average relative power was -0.65 in the receiver antenna array. The experimental ARP results agreed with calculated results from the derived mathematical model of the portable BMS system, by 80% when considering the phase angle and by 85% without the phase angle. The preliminary results are promising and provide some insight as to where improvements must be made to enhance the detection ability and to reduce the differences between simulation and experiment results of the portable system.

CONTRIBUTIONS

The primary contributions of the author of this thesis are reported in the following section:

- This dissertation focuses on the development and evaluation of a microwave sensor array for a portable breast cancer detection system. The system's development included the design and/or evaluation of the receiver antenna array, the RF detector selection, and the switching circuit build for data acquisition.

- A single receiver antenna was characterized at different distances from the transmitter (horn antenna), and the symmetrical analysis of the receiver's semicircular platform was analysed using two receiver antennas.

- The optimal separation between each antenna in the receiver antenna array was determined, and the array was built and characterized. Conjointly, the switching circuit was designed by a summer student, Justin Roznik.

- The gain and bias factors were calculated for 13 sensors at 10 frequency points from 1.5 GHz to 6 GHz at intervals of 0.5 GHz. The receiver sensors were calibrated by applying simulation results generated by Debarati Nath using CST Simulation Studio 2019.

- The differences between the experimental and simulated power for a free air system and with an Aluminum rod placed at different positions in the scanning plane were obtained. A sensitivity analysis of the system for a point like a scatterer (Al rod) in the scanning chamber was carried out.

- A mathematical model for the portable system (derived by Pistorius) was compared to the experimental results for the point-like scatterer in the scanning chamber.

ACKNOWLEDGEMENTS

He who does not thank the people, does not thank Almighty Allah.

–Prophet Muhammad (may peace be upon him)

First and foremost, praise is to Almighty Allah (SWT) for all His blessings for giving me patience and good health throughout my MSc degree.

I would like to give my sincere thanks to my academic supervisor, Dr. Stephen Pistorius, who supported, guided, and encouraged me during my studies. An email conversation with Dr. Pistorius almost three years ago commenced me on the journey that brought me to Canada. I am grateful forever for your comments and suggestions that helped me to learn new lessons and improve my research knowledge.

I would also like to acknowledge my colleagues at the Non-Ionizing Imaging research group for the support and fruitful discussions we had together for the two years and hopefully will continue to have in the future. Special thanks for Mario Solis-Nepote, who provided me generous and valuable mentorship during my graduate studies. I also thank the summer student (Justin Roznik) for his help during the summer of 2019.

I would like to express my high appreciation and thank my M.Sc. committee, Dr. Puyan Mojabi, Dr. Sherif Sherif, for their advice and comments to improve this work. I extend my thanks to the support staff at the Graduate Program in Biomedical Engineering and the Department of Physics and Astronomy at the University of Manitoba.

I extend my gratitude to the CancerCare Manitoba Research Foundation and the Manitoba Graduate Fellowship program for their financial support.

Finally, I would like to thank my parents, family, and friends everywhere for all your support and patience.

DEDICATION

To my parents, nothing would have been possible without their constant love and support. And my supervisor Dr. Stephen Pistorius, who guided me to achieve my goals.

TABLE OF CONTENTS

LIST OF TABLES

LIST OF FIGURES

LIST OF ABBREVIATIONS

BMS	Breast Microwave Sensing
MRI	Magnetic Resonance Imaging
US	Ultrasound
VNA	Vector Network Analyzer
MWI	Microwave Imaging
EMW	Electromagnetic Waves
MWT	Microwave Tomography
OI	Object of Interest
UWB	Ultrawideband
FDTD	Finite Difference Time Domain
TSAR	Tissue Sensing Adaptive Radar
BAVA-D	Balanced Antipodal Vivaldi Antenna with a Director
FEM	Finite Element Method
CSI	Contrast Source Inversion
ABS	Acrylonitrile Butadiene Styrene
DAS	Delay and Sum
DMAS	Delay Multiply and Sum
CNN	Convolutional Neural Network
MoM	Method of Moments
SSVA	Side Slotted Vivaldi Antenna
MLP	Multi-Layer Perceptron
AUC	Area Under the Curve
SD	Standard Deviation
ECC	Envelope Correlation Coefficient
NDD	Normalized Different Distance
PCC	Printed Circuit Board
RF	Radio Frequency
CW	Continuous Wave
MIMO	Multiple Input and Multiple Output
ANOVA	Analysis of Variance
CI	Confidence Interval

RP   Relative Power

ARP   Average Relative Power

CHAPTER I

INTRODUCTION

1.1   Introduction

Cancer is the world's second leading cause of death, and an estimated 9.6 million people died from different kinds of cancer in 2018 [1]. Breast cancer is one type of cancer that affects 2.1 million women in the world annually and causes more deaths of women than any other malignant neoplasm [2], with more than 626,027 people dying annually worldwide due to this disease [2]. The mortality rates have increased in many countries in Asia, Africa and Latin America [3]. The 5-year breast cancer survival rate for women in 2010-2014 was 65% in Malaysia and India, while it was 90% in the United States and Australia [4]. In Canada, during 2018, about 8% of all cancer-related deaths were due to breast cancer [5]. The same study identifies that in Canada, the breast cancer mortality rate in females declined from 48% to 22.4% from 1994 to 2015. Early-stage breast cancer is a treatable disease, with early-stage detection increasing the overall survival [6]. The survival rate can reach as high as 97% with early detection, which emphasizes the need for an efficient and reliable diagnostic technique for early breast cancer detection [7]. According to the different statistical findings, survival rates can be increased by early detection and the availability of breast cancer screening technologies.

1.2   Breast Anatomy and Cancer Classification

Understanding the anatomy of breast cancer plays a vital role in building the breast cancer detection model. The anatomy of the breast with its surrounding tissues is shown in Figure 2.1 [8]. In general, the breast has no muscle but is composed of skin, fat, connective tissue, and glandular tissue. The breast attaches to the chest wall with a circular base of diameter between 7 to 8 cm [9]. Each breast has many smaller spaces known as lobules

(glands), which in turn are formed from 15 to 20 lobes [10]. There are bulbs at the end of each lobule which can produce milk, and ducts carry milk from lobules to the nipple [10]. Cancerous cells occur due to uncontrolled cell growth and cell mutation [8]. Cancerous cells can invade and damage the surrounding tissues. In general, breast cancer is broadly divided into non-invasive and invasive categories. Non-invasive cancers stay within the breast and do not metastasize beyond the breast. On the other hand, invasive cancers can spread into adjacent and distant normal healthy tissues. Most breast cancers are invasive [11].
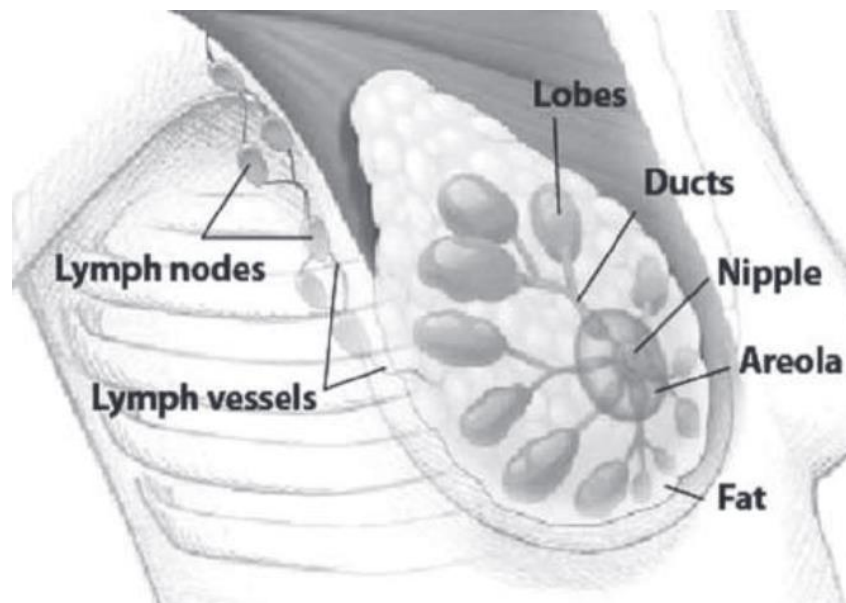
Figure 2.1   Anatomy of Human Breast [8].

1.3   Challenges with Current Modalities

Screening for breast cancer is a common technique to detect cancer before symptoms affect the subjects. A manual breast exam can be done using a hand to check for any changes in the breast texture to identify abnormally growing cells [12]. Presently, three imaging techniques exist for breast screening applications, i) X-ray mammography, ii) Magnetic Resonance Imaging (MRI), and iii) Ultrasound (US) Imaging.

X-ray mammography is the current standard for early-stage breast cancer detection. However, this technique has many drawbacks. These include:

a) the use of ionizing radiation, which can raise the risk of carcinogenesis and requires breast compression [13],

b) low sensitivity as it has been shown that for x-ray mammography that up to 15% of cancer lesions are missed in dense breasts [14], and

c) less than ideal specificity, as the false-positive rate is about 10% for the patients, which leads to additional imaging and biopsies [15]

d) high cost and structurally sensitive as it is not ideally suited to the rigours of screening in remote locations and developing countries [13].

Ultrasound imaging uses non-ionizing high-frequency soundwaves and provides good imaging resolution screening technique for breast cancer detection [16]. However, it has a 65.5% specificity rate [17], and the diagnostic procedure requires a radiology expert both to perform and interpret the image [18]. It has been concluded that X-ray mammography, either on its own or combined with Ultrasound, is inadequate for breast cancer detection of women with a higher risk due to a history of hereditary breast cancer [19].

Though Magnetic Resonance Imaging (MRI) is a non-ionizing and more sensitive screening technique than X-ray mammography, but it is expensive and time-consuming [20]. MRI is also unsuitable for patients who have claustrophobia [20], and similar to Ultrasound, MRI has a poor specificity, which makes it unsuited for breast cancer screening[17].

In the last decades, numerous researchers have started to investigate non-ionizing microwave technologies as a complementary modality for early breast cancer detection. Microwave imaging techniques do not use ionizing radiation and cost-effective compared with conventional imaging modalities.

1.4   Breast Microwave Imaging

In microwave technology, images are produced by the backscattering of electromagnetic signals within the microwave range from the object of interest. Currently, microwave imaging has been used for the diagnosis of bone lesions, brain hemorrhages, liquid in the lungs, the urine volume in the bladder, and breast cancer [21]. This imaging modality is relatively new in biomedical applications and needs the technological development of custom hardware for clinically approved.

Microwaves are sensitive to the dielectric contrast between healthy and cancer cells, and this is the key factor in exploiting microwave technology for breast health monitoring [22]. The electrical properties (permittivity and conductivity) of a given cell have a mutual

connection with their water content and ionized molecules in the cell. Cancer cells have a higher dielectric constant due to their higher water content than healthy cells [23].

Microwave imaging is a growing technique for detecting dielectric bodies and scrutinizing the cancerous breast lesions as compared to other body organs. Custom build receivers with a commercial vector network analyzer (VNA) system can detect signals as weak as -140 dB down from the initial inserted signal [24]. Thus, while microwaves can penetrate to a depth of around 100 mm, a possible breast radius, suffice to attenuate a 10 GHz signal by more than 80 dB, they cannot access other organs like the kidney or liver [25]. Secondly, unlike internal organs, the breast has no muscle layers, which helps lower the scattering and signal attenuation. An array of antennas can be rotated from zero to 360 degrees around the breast, and both transmitted and backscattered reflection from the breast can be recorded. Thirdly, microwave imaging permits frequent inspection for early diagnosis without harmful radiation dose because it uses low-power non-ionizing radiation. Finally, the electrical properties (conductivity and permittivity) help create a reflectivity map as a function of position, showing the healthy and cancer tissue inside the breast.

The permittivity depends on the water content in the cell, while conductivity is mostly related to the presence of ionizing molecules, like salt [24]. Due to the growth of angiogenesis (blood vessels), cancer cells have a higher water content concentration [21], and thus, cancerous tissue has greater permittivity than normal healthy cells. The ratio between permittivity of cancer cells and normal healthy cells, known as contrast, is frequency-dependent and decreases at shorter wavelengths [24]. Measuring the electrical properties of biological tissues is a challenge. Information about water content or the presence of a tumour can be obtained by measuring the electrical properties of the tissues.

In vivo, measurements are an invasive surgical procedure for the measurement of tissue properties. Tissues become dehydrated due to their removal from the body. Thus, the properties may change if they are measured outside the body. Early studies found that the contrast may be greater than a factor of 10 between tumour and breast tissues [26]. However, more recent studies have shown that this contrast is only applicable between adipose tissue and tumour, while the contrast is 40% lower between fibro glandular tissue and tumour [27]. Sugitani et al. carried out an ex-vivo measurement on 35 patients in the rage of 0.5 GHz to 20 GHz and

reported that the dielectric properties of tumours[1] to be six times greater than those of fatty tissue and 1.5 times higher than fibro glandular tissue [28]. The study reported that the contrast between tumours and fibro glandular tissue varied from 8% to 15% [28], while X-ray mammography has a lower contrast of 4-10% [24].

1.5 Microwave Imaging Advantages and Disadvantages

1.5.1 Advantages

Microwave technology is risk-free for patients due to its use of non-ionizing radiation. Therefore, diagnosis can be repeated more frequently [29]. It is also more comfortable for patients because there is no painful compression of the breast during the examination as like X-ray mammography [15]. Microwave technology has the advantage of a high detection rate and low cost. Due to the high contrast between dielectric properties of healthy and malignant breast tissues over microwave frequencies, microwave imaging (MWI) offers an alternative pathway for mass population breast screening [24].

1.5.2 Disadvantages

Microwave tomography and radar-based microwave imaging are the two most common imaging modalities in microwave technology. The main limitation of tomography-based microwave technology is to reconstruct the dielectric profile from a non-linear and ill-posed inverse algorithm [30]. Current tomography-based microwave techniques are computationally expensive and can take hours or days to generate a reconstructed image. A single frequency band is necessary to reduce the complexity of the model [31]. The authors concluded that the presence of tumour in the reconstructed image was found to be challenging where the volume of the glandular fraction (VGF) in the breast was high [30]. Radar-based models do not consider the electromagnetic scattering, antenna beam pattern and frequency-dependent gain,

---

[1]A tumour is a lump or mass of abnormal tissue that develops when cells reproduce too quickly. A tumour can be of two types: benign and malignant. Benign tumours are not harmful, and they do not spread to other parts of the body. Malignant tumours are cancerous, which can grow and damage healthy cells. While breast microwave sensing systems have the potential to recognize both benign and malignant tumours in the breast, in this thesis, the term tumour will be used to describe a cluster of cancer cells located in the breast.

signal attenuation and dispersion within the breast, and other path-dependent or system-specific effects. Despite the increased number of probing locations, low image contrast is still a challenge for air-based radar systems [32]. Both microwave imaging modalities have intrinsic weaknesses in the resolution of the reconstructed image, particularly within the glandular region [24].

1.6   Problem Statement

Breast cancer statistics show that the incidence rate has accelerated in low to middle-income countries and rural communities [4]. Most breast cancer screening systems are currently designed for use in an urban/clinical environment and require an experienced technician and radiologist to review the images. For use in remote regions or developing countries, another approach is needed. An ideal breast screening technique would be portable, so that it can be easily moved from one location to another, would have a low manufacturing and operating cost, and could be used for mass screening without the need for highly trained operators or radiologists.

The work presented in this thesis is focussed on the development of RF hardware associated with a portable Breast Microwave Sensing (BMS) system. The BMS system has been designed by building on different approaches and ideas from other researchers and aims to maximize portability and minimize cost, without compromising the diagnostic capability. In 2017, Jorge A. Sacristán from Dr. Pistorius's non-ionizing imaging laboratory simulated a portable system to show that machine learning could be used to detect the presence of a breast lesion. This portable prototype system consisted of a rotating rectangular shaped chamber with a point like microwave source and twelve microwave receiver sensors. While the simulated prototype system demonstrated that such a system is feasible using different machine learning approaches to detect breast cancer, experimental and clinical validation is still required. This work aims to develop a sensor and antenna array with optimal separation between each receiver antenna and to evaluate the potential performance of the sensory array experimentally. The dimension of the array depends on the size and mutual coupling characteristics of the antenna elements. The MWI approach uses scattering parameters to reconstruct an image from backscattering signals. The backscattering signals from the breast are rectified into an output voltage through a microwave detector, and the measured output voltage can then be classified using machine learning to detect cancerous lesions.

The objective of this thesis was to examine the requirements for an array of sensors for portable breast microwave sensing systems, specifically, the number of commercial Ultrawide frequency band antennas, the optimal antenna spacing, and the required characteristics for microwave detectors with more than 140 dB dynamic power range. This study is also needed to determine the accuracy and quantify the errors of the systems for future prototypes and diagnosis. The portable sensing system was calibrated by applying parameters such as bias factor, gain from the sensor, and the geometric correlation constant from the simulation in microwave CST studio (version 2019). Finally, a mathematical model was derived for the BMS system to determine the impact of the position of an Al rod (simulating an ideal tumour response) using an inverse problem.

CHAPTER II
LITERATURE REVIEW

2.1   Introduction

The previous chapter provided the enumeration of breast cancer incidence and death rates as well as the current standard techniques for breast screening. Mortality rates depend on the availability of breast cancer screening. The main benefits and drawbacks of the current breast cancer screening techniques were described, and the summary of microwave imaging for breast cancer detection. The portable breast microwave sensing system is not ready for experimental and clinical practice.

The main goal of this thesis was the development and testing of an antenna array for a prototype portable microwave sensing system. This chapter presents the technical details of the existing microwave-based breast cancer screening systems. In particular, the different hardware approaches used the antenna design, array formation, hardware setup, and mechanical structure are presented. The last section of this chapter summarises the simulation-based portable breast cancer detection prototype developed by our research group. The key objective of this chapter is to provide a comprehensive account of the latest advances in electromagnetic tools and techniques for microwave technology.

2.2   Microwave Based Technologies

Microwave based technologies have become a novel candidate to overcome the problems of X-ray mammography. Microwave based technology is being widely used to diagnose human health, and microwave imaging (MWI) is a promising modality for breast cancer screening [33]. Microwave imaging uses electromagnetic waves (EMW) with frequencies in the 300 MHz to 30 GHz range to observe or detect unseen or inserted substances in a media by mapping the distribution of the electrical property in an object [34].

There are two approaches to microwave imaging. The first is Microwave Tomography (MWT), and the other is Radar-based Imaging. Tomography is a quantitative imaging modality in which a map of electrical properties of an object of interest (OI) is reconstructed from electromagnetic field measurements. Image reconstruction is achieved by solving the non-linear and ill-posed inverse scattering problems.

Semenov has recently reviewed MWT for various biomedical applications. He concluded that MWT could provide quantitative images that can be useful in evaluating tumour progression or regression in the breast [35]. The Electromagnetic Imaging Laboratory at the University of Manitoba has built a 3D full-vectorial prototype for breast cancer detection system with 120 microwave transmitter/receivers and liquid (e.g., water) as a coupling medium within the imaging chamber. Their prototype has been evaluated using several microwave tomographic imaging approaches [36].

Radar-based imaging is the second MWI approach and produces 2D or 3D images of an object of interest (OI). In radar-based imaging, an antenna transmits an electromagnetic wave to illuminate an OI. The electromagnetic waves will scatter within the OI and reflect the signal to one or more antenna. The reflected signals are used to create a reflection map that can be displayed as an image. The resolution depends on the operating frequency bandwidth of the radar-based system. Frequency selection for radar-based systems involves a trade-off between image resolution and penetration power. Higher frequencies have lower penetration power but offer a higher intrinsic resolution. Likewise, low frequencies provide less spatial resolution but provide deeper penetration. James C. Lin showed theoretically that the ideal frequency range of microwave imaging of biological tissue should be from 2 to 8 GHz when accounting for resolution and attenuation inside the body [37]. Radar-based imaging modality has inherent sensitivity limitations to small and low contrast objects [38].

2.3   Current State of Clinical Systems for Breast Microwave Imaging

There is a relatively small number of research groups working on microwave breast imaging for breast cancer detection. Dartmouth College, the University of Calgary, the University of Bristol, and McGill University have reported clinical results. At the University of Manitoba, the Non-Ionizing Imaging research group led by Dr. Pistorius has developed a Health Canada licensed medical device for clinical breast MWI and has completed a Phase 1 clinical trial.

In this section, the technical aspect of the systems chosen by each group is reviewed, namely the types of antennas and their operating frequency ranges, the image reconstruction algorithms used as forward solvers, and the hardware setup. The characteristics of the system are summarized in Table 2.1.

Table 2.1   State-of-the-art, microwave breast imaging systems.

	Dartmouth College	University of Calgary	University of Bristol	McGill University	University of Manitoba
Antenna Setup	16 antenna arrays with mechanical movement	Balanced Single antipodal Vivaldi antenna with vertical movement	60 Ultrawideband (UWB) antennas	16 antennas	Two horn antennas
Operational Frequency	250 kHz to 3 GHz	0.05 GHz to 15 GHz	3 GHz to 8 GHz	2 GHz to 4 GHz	1 GHz to 8 GHz
Scan Platform	Cylindrical chamber (Agar gel, corn syrup, water mixer).	Tank with canola oil.	Hemispherical ceramic cup	Hemispherical ceramic radome	Air operation
Object of Interest	Detecting cancer cells in the breast.	Pilot clinical experiment.	Symptomatic Patients.	Clinical testing.	11 healthy volunteers and 3D phantoms.
Modality and Result	Tomographic, 2D and 3D images.	Radar-based, monostatic and Consistent Images.	Radar-based, multistatic, low resolution, clutter rejected images.	First experimental microwave time-domain study with real volunteers.	Radar-based mono, multistatic and Reconstructed 2D image.

2.3.1 **Dartmouth College**

Meaney et al. from Dartmouth College in New Hampshire, USA, presented the first clinical prototype of a near-field BMI system in 2000 [39]. In 2014, they published the third generation of their system [40]. That system uses sixteen elements of a transceiving monopole antenna array with an operating band from 0.5 to 3 GHz. The monopole antenna array is connected to a 16-channel switching matrix and a digital radio-frequency generator. The

antenna array is housed in a chamber filled with water and glycerin mixture liquid as the coupling medium to mitigate reflections from the skin surface.

The antenna array scans the breast at several adjusted heights, using a hydraulic jack located underneath the array. A Finite Difference Time Domain (FDTD) algorithm is used to reconstruct images from measured near-field signals. This reconstruction is not affected by the diffraction limit. However, FDTD can be slow to compute for 3D model reconstruction. Also, the FDTD model does not work well with oddly shaped targets, for example, the nipple [41].

2.3.2 University of Calgary - TSAR

The research group at the University of Calgary carried out their first pilot clinical trials and published an article describing their breast MWI system in 2012 [42]. They use a monostatic radar-based technique, known as tissue sensing adaptive radar (TSAR). A custom Balanced Antipodal Vivaldi Antenna with a Director (BAVA-D) is used to build the monostatic system with vertical scanning. The custom antenna covers the operating bandwidth from 2.4 to 12 GHz [43]. The antenna is attached to an arm inside a tank filled with a matching liquid to minimize the reflections from the skin interface. This mechanical arm permits perpendicular movement over a length of 24 mm to 141 mm. The tank is filled with canola oil, and the arm scans on a cylindrical geometry that circumambulates the breast.

A laser and camera are used to find the separation between antenna and breast. The laser outlines the breast. A patient lies on a bed in the prone position, and the bed has a 130 mm opening for the breast, which is immersed in the canola-oil filled tank. The antenna scans the breast at 200 positions in 30 minutes. An FDTD simulation microwave solver is used to simulate a breast phantom, the BAVA-D antenna, and the tank filled with matching liquid. Simulated data are compared with measured data to validate the TSAR system [44]. An outline of the target is made by using the radar algorithm. A finite element contrast source inversion (FEM-CSI) algorithm has used this information as the starting point and reconstruct a higher resolution image [38].

2.3.3 University of Bristol – MARIA M4

The University of Bristol has developed a series of prototype MARIA multistatic radar-based scanner for breast cancer detection [45]. Their generation prototypes have advanced from

early systems with an ultrawideband (UWB) slot array with 16 antennas to a 31-antenna array system (MARIA M3). Their latest generation system MARIA M4 has been designed using a new UWB array with 60 antennas arranged in a hemispherical fashion. This hemispherical cup is made of acrylonitrile butadiene styrene (ABS) plastic. The MARIA M4 system operates in the frequency range of 3 to 8GHz. The antenna array enhances the number of measurements by a factor of approximately four and measurement speed from their previous two prototypes [46]. A low-loss ceramic shell with a dielectric constant of 10 has been used as the coupling between the antenna array and the breast [45]. There is a space in this shell between the antenna face and different materials. Space is filled with water or oil-based coupling fluid with a dielectric constant of 10. The Bristol group uses a modified version of the classical delay-and-sum (DAS) beamforming algorithm to generate the image.

2.3.4 McGill University

In 2014, the research group at McGill University in Canada had built a time-domain multistatic radar system of bandwidth from 2 to 4 GHz and a hemispherical dielectric bowl [47], [48]. An antenna array of 16 elements has embedded in the hemispherical dielectric bowl—the antenna array oriented in such a way that help to measure both co-polarized and cross-polarized information. A pulse generator transmits a time-domain Gaussian signal of 70 ps duration with its main frequency content range from 2 to 4 GHz. The short duration pulse is fed to the antenna array and propagates in the breast. A switching network uses to select one antenna as a transmitter and the other 15 as receivers. The scattered signal from the breast is received by the remaining 15 antennas, and the received signal is recorded in an oscilloscope. The process is repeated until each antenna in the array acting as a transmitter. A total of 240 signals is recorded from one time scan the breast for all possible antenna pairs. A Coupling liquid (Ultrasound gel) with a dielectric contrast of 68 is used to fill the air gaps between the breast surface and the hemispherical radome. The recorded data is then filtered to remove background noise and reflections. Finally, the delay-multiply and sum algorithm (DMAS) is applied to obtain 3D images. The proposed system reduces measurement ambiguity and noise.

2.3.5 **University of Manitoba**

In 2017, the non-ionizing imaging research group at the University of Manitoba developed a bistatic radar-based breast microwave imaging system with a 2 to 8 GHz bandwidth [21]. A bed with an aperture of 17 cm for one breast is used during the scan to support the volunteer in the prone position. The system uses two double-ridged horn antenna array, which has the bandwidth from 2 to 20 GHz. The antennas are placed on the circular tabletop by the holder with 35, 145- or 180-degrees angular separation. The system operates in an air medium to reduce the mechanical complexity and losses associated with coupling liquids. A complete scan depends on the combination of three vertical planes with 144 antenna positions, and a scan can be completed in 1755 s to 1876 s. The scattering and reflection data are recorded using a two-port Planar Vector Network Analyzer (VNA). An iterative Delay and Sum (itDAS) reconstruction algorithm or a Deep Convolutional Neural Network (CNN) is used to image and detect the presence of cancer in the breast [49].

2.4   Types of Antenna used in Microwave Breast Imaging Applications

Hagness et al. 1999 [50] investigated an ultrawideband (UWB) radar-based microwave technology to detect early-stage breast tumours. A resistively loaded bowtie antenna was designed using a Finite-Difference Time-Domain (FDTD) simulation solver. The antenna acts as a transceiver in the system. The researchers concluded that the system could successfully detect small tumours, which are usually missed by X-ray mammography, by combining existing equipment [50].

In 2007, Nilavalan et al. [51] designed a stacked Ultrawideband (UWB) patch antenna for the detection of breast tumours. The designed antenna is simulated in Finite-Difference Time-Domain (FDTD) simulation models and compare those results with a physical prototype. The antenna operates from 4 GHz to 9.5 GHz frequency. A phantom made of synthetic breast tissue was scanned to measure the radiation properties of the antenna. A prototype of the antenna was immersed in the breast tissue medium, and an identical second prototype was placed over the horizontal plane in the air-medium interface.

In 2010, Zhurbenko et al. [52] developed a multichannel 3D architecture of a microwave imaging system with 16 pairs of identical transceiver channels. A thirty-two monopole antenna array was simulated using a Method of Moments (MoM) forward solver.

Their designed monopole antenna operated from 0.3 GHz to 3 GHz. The antenna array is placed in a cylindrical setup to collect the data. The images are generated using a non-linear inverse scattering-based image reconstruction algorithm. This algorithm is a combination of the moment forward solver method and the Newton minimization algorithm.

In 2013 [53], an array configuration of 12 corrugated tapered slot antenna elements for UWB based microwave imaging systems was reported to attain a low profile with moderate gain. Though the functioning of the antenna is satisfactory, the antenna is a 110 cm in width, and the substrate named Rogers RT6010 has dielectric constant of 10.2. In simulation results, the working bandwidth started at approximately 5 GHz, which made the antenna unfit to use at lower frequencies.

J. Bourqui *et al.* [43] has presented a balanced antipodal Vivaldi antenna for the detection of breast cancer, focusing on the UWB tissue sensing adaptive radar system. The antenna design originates from the design of a balanced antipodal Vivaldi antenna. The custom antenna covers an operating frequency from 2.4 to 12 GHz.

Islam designed a modified Side Slotted Vivaldi antenna (SSVA) in 2017 [54]. The antenna is modified by cutting six side slots in the radiating fins. These slots enhance some antenna properties such as the electrical length, efficiency, improved radiation directivity with high gain. Side slot cutting attempt reduces the lower sideband of bandwidth without affecting the dimensions of the antenna. The first resonant frequency occurs at 1.79 GHz, and the overall size at this frequency is about $0.4\lambda \times 0.5\lambda$. The fractional bandwidth is about 127% from 1.54 to 7 GHz for S11<-10dB.

2.5   Present State of Portable Breast Microwave Sensing System (BMS)

In 2017, J. A. Sacristán from the non-ionizing imaging research group at the University of Manitoba simulated a portable mobile Microwave Breast Cancer Detection Device and showed that it was feasible to detect breast lesions using Machine Learning [55]. The work discussed in [55] was a proof-of-concept using a forward model with twelve solid-state microwave sensors as the receivers and assumed a point-like source as a transmitter. The authors simulated three datasets based on breast tissue structure, tumour radius, and the rotation of the transmitter antenna. The Multi-Layer Perceptron (MLP) neural network algorithm detected the presence of tumours from the heterogeneous dataset with the area under the curve (AUC) of $(86 \pm 2)\%$. The work in [32] covers the development of a portable breast microwave

sensing system, which has a small footprint, lightweight and robust construction and no need for impedance matching liquid. In preliminary studies, an $(83 \pm 2)\%$ sensitivity rate and $(91 \pm 2)\%$ specificity rate for abnormalities in low-density breast phantoms has been achieved.

2.6   Summary

The current chapter has discussed an up-to-date detailed review of microwave imaging systems. The importance of a new Breast Microwave Sensing (BMS) system has been mentioned in this chapter. The development and evaluation of a portable BMS system will be discussed in the next chapter with the characterization of the antenna array.

CHAPTER III
METHODS AND MATERIALS

3.1   Introduction

The previous chapter discussed the hardware setup and image reconstruction techniques of current clinical breast microwave imaging systems. The clinical breast MWI systems are hard to move due to the complex and large hardware setup. The main goal of this work is to design, develop and evaluate the performance of a new portable system. This chapter explains the detailed methodology of designing, developing, and validating the proposed portable breast microwave sensing (BMS) system to detect tumours inside the breast. System requirements and each component are described in the first section of this chapter. Next, the antenna array design and the construction process are presented. This chapter is an effort to provide a clear and useful idea of developing a portable BMS system for breast cancer detection. The last section of this chapter details the experiments conducted to calibrate and validate the antenna system for detecting a point-like scatterer.

3.2   Prototype Design and Construction

In 2017, Jorge A. Sacristán [55] examined some feasible constraints for a portable Breast Microwave Sensing (BMS) system and designed a prototype. The BMS system has the following constraints:

1. The whole BMS system can be fitted in a piece of luggage, not bigger than 55 cm $\times$ 55 cm $\times$ 55 cm.
2. The overall system weight should less than 25 Kg.
3. The BMS system can scan most breast sizes.
4.   Instead of trained personnel, an automatic classifier is used to detect the presence or absence of a tumour in the breast.

The main design objective of a portable BMS system requires an apparatus setup that is easily transported by personnel in a remote area. The first two constraints concentrate on the main constructional development goal of this framework. Current clinical breast microwave imaging (BMI) systems were discussed in Chapter 2 and do not meet these constraints due to the use of microwave compatible beds, microwave switching circuits, and tanks for matching. The clinical approaches may conflict with the portable system model, as they typically require large and heavy equipment.

Fu et al. [56] and Cao et al. [57] published papers describing the use of mm size solid-state spintronic sensors for microwave imaging. These sensors can rectify both E-field and H-field radiation into a DC voltage. To illuminate the target, a standard X-band horn antenna was used as a transmitter. The spintronic sensors 15 cm away from the target received the reflected signals. Furthermore, this system demonstrated the ability to use small sensors, operating at microwave frequencies in the near and far-field, to create images. Based on these techniques, a rectangular rotating chamber was built to contain one transmitting antenna and several microwaves receiving sensors.

The system mentioned in [44] had a breast aperture of 13 cm in diameter. Nevertheless, an earlier study found that the mean breast diameter (± standard deviation) was 13.7 cm ± 0.2 cm for D-cup breasts [9], the mean breast length measured from the chest wall to nipple in the pendent position was 9.7 cm ± 0.2 cm [9]. To accommodate a broader range of breast sizes (the third constraint of the list), for the breast aperture and chamber depth respectively, a 15 cm diameter and 15 cm height were chosen.

The fourth constraint in the list removed the requirement for a Radiologist to diagnose a tumour in either Microwave Tomography (MWT) or Radar-based Imaging. The BMS system has a machine learning-based automated classifier and on-screen instructions, which direct the individual using the system as to what to do, and finally identifies the classifier's prediction of the presence or absence of a tumour. The portable BMS system is designed based on these constraints and shown in Figure 3.1.
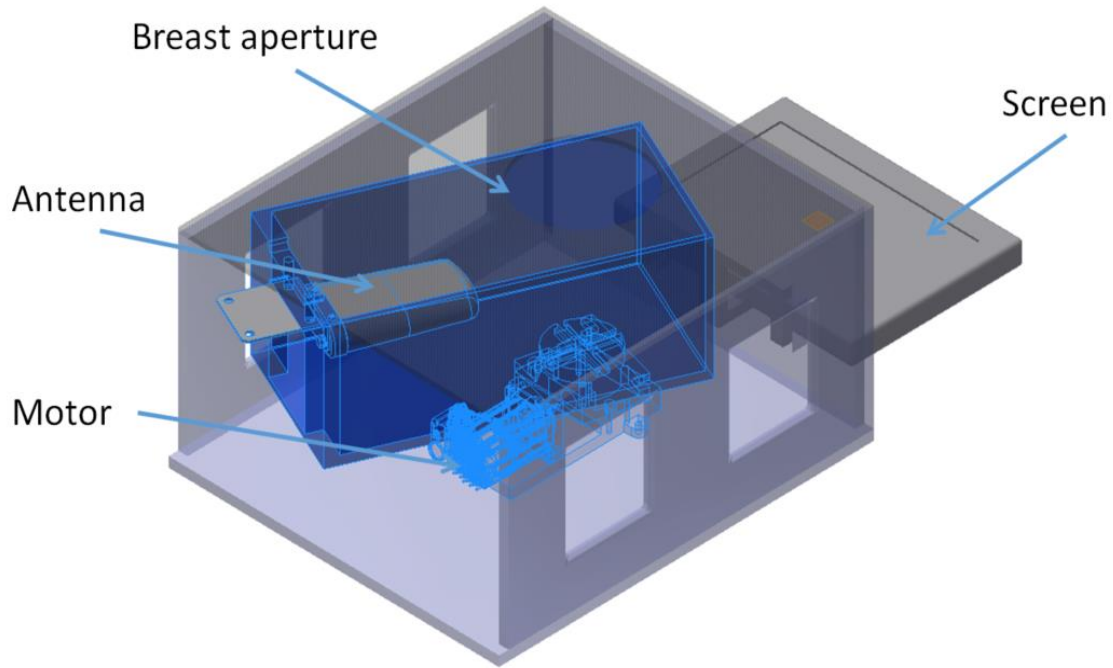
Figure 3.1   Three-dimensional view of the BMS system. The inner chamber is rotated around the breast using the servomotor. The servomotor is mounted at the center of the breast aperture, and a user can follow instructions on the screen [55].

3.3   Methodology

Initially, the hardware construction and assembly will be briefly described. Each component utilized in the proposed system, along with its specifications, is presented in the first subsection. Next, the reduction of mutual coupling between the receiver antenna by Envelope Correlation Coefficient (ECC) is presented. Following that, the receiver antenna array was built, and the time dependency of each sensor was determined. The measurement and system calibration methods are also described. Afterward, a point-like (e.g., Aluminum Rod) was used to measure the sensitivity of the developed portable system. Finally, the analytical model that was developed to describe the relative response of the electric field at each antenna to a point-like scatterer (e.g., Aluminum Rod) will be described. The steps of the proposed methodology to develop a portable BMS system is described in Figure 3.2.

```
            ┌─────────────┐
            │    Start    │
            └─────────────┘
                   │
                   ▼
```

Initial Study:
1. Identify the Current Issues
2. Find out Related Problem

Literature Review:
1. Understanding the Current Research Trends, Issues and Feature of Antenna, Breast Cancer Detection
2. Get Antenna Specification
3. Get RF Detector Specification
4. Review on the Experimental Analysis and Factors relating to Breast Cancer Detection System

Methodology:
1. Receiver Antenna and RF Detector Selection
2. Antenna Characterization
3. Internal Scanning Chamber Build
4. Mutual Coupling Effect Reduction
5. Receiver Antenna Array Build and Characterization
6. Time Dependency Test ANOVA Analysis
7. Comparison between Simulation and Experimental Work
8. Modelling of the Developed Portable System

Prototype Development and Measurement:
1. Switching Circuit Build
2. Scattering Power Measured as Voltage from the RF Detector

Results and Discussion:
1. Single Sensor Characterization
2. Receiver Antenna Separation Calculation
3. Time Dependency Results of the Antenna Array
4. Gain Calculation
5. Comparison Between Measured Voltage and Calculated Voltage from Simulated E-field
6. Sensitivity Result of the Developed System
7. Mathematical Model Discussion for a Point Like Scatterer in the Scanning Grid

```
            ┌─────────────────┐
            │ Conclusion and  │
            │ Recommendation  │
            └─────────────────┘
```

Figure 3.2   Flowchart for the portable BMS system hardware development.

3.3.1 **Receiver Antenna Selection**

The initial part of the antenna selection process is the collection of targeted specifications according to the application of the microwave system. Researchers identified several antenna properties that are suitable for successful microwave technology. Radiation patterns, penetration power, and small dimensions to make the system portable are the most desired specifications [58]. Furthermore, the number of elements of an array can be limited by the receiver dimensions and electromagnetic crosstalk properties. Currently, researchers are working to achieve optimum antenna efficiency within the compact dimension. Frequency selection is a critical factor for microwave applications. The lower the antenna's operating frequency band, the greater signal penetration power, and less signal attenuation can be obtained [24]. Above 10 GHz operating frequency give high signal attenuation and less penetration [24]. Authors in [37] claims that 1 GHz to 8 GHz bandwidth provides the optimal balance between signal penetration and attenuation. High sensitive broadband antennas are useful when there are large penetration losses due to the object of interest in the microwave imaging application [59]. Nine commercial antennas were tested in the air medium at the laboratory. Among them, the 146184 UWB dual-band PCB antenna with balanced transmission antenna shown in Figure 3.3 from the Molex Company exhibits superior performance for different distances from the transmitter horn antenna in the air medium [60]. The characteristics of the dual-band PCB antenna with balanced transmission antenna are provided in Chapter Four as a function of frequency. The properties of the receiver antenna for the portable BMS system are summarized in Table 3.1.

Table 3.1   Properties of receiver antenna for the portable BMS system.

Parameters	Requirement	146184 UWB
Operating Frequency	The lower band covered wideband	2 GHz to 6 GHz
Radiation Pattern	Unidirectional	Unidirectional
Efficiency	High ($> 70\%$)	$> 66\%$
Directivity	Unidirectional	Unidirectional
Polarization	Linear	Linear
Physical Dimension	Compact	4.70×1.76 cm

Figure 3.3   Physical dimension 146184 UWB-ready dual-band PCB antenna with balanced transmission cable [60].

3.3.2 **RF Detector Selection**

The selection of a Radio Frequency (RF) detector is highly dependent on the transmit and measure the signals radiated power in the portable BMS system. Electromagnetic waves can be detected by an RF detector through either wireless or wired (on RF Cable) physical transmission medium. An RF detector detects or measures the power of an RF circuit and produces a dc output voltage relative to the input electromagnetic power. An RF detector is a rectifier/low pass filter circuit that converts the received microwave signal to a dc output voltage. The dc output voltage for 10 dBm transmitted power is in the millivolt range, and an instrumentation amplifier amplifies this signal. RF detectors are specified to work over a particular dynamic range and a frequency band. They respond within a nanosecond fall or rise time of the input RF signal to obtain an accurate power level. In our BMS system, a dual-channel RF detector (ADL5519, shown in Figure 3.4) is used. The ADL5519 is a logarithmic amplifier designed with six cascade-connected gain demodulating stages [61]. It can rectify an electromagnetic signal into a dc signal from 0.1 GHz to 10 GHz. The overall dc gain is high because of the cascaded nature of the gain stages. At the output of each gain stage, a square-law detector cell is used to rectify the signal. The dc output voltage has an inverse relation with the input RF power. The RF detector has an internal temperature sensor that provides a scaled voltage, which is proportional to the temperature from - 40°C to 125°C. The key features of the ADL5519 are summarized below:

- Bandwidth: 0.1 GHz to 10 GHz.

- 62 dB dynamic range.

- Dual input and dual output ports.

- Temperature stability: ±0.5 dB (- 40°C to +85°C).

- Power supply range 3.3 V to 5.5 V.
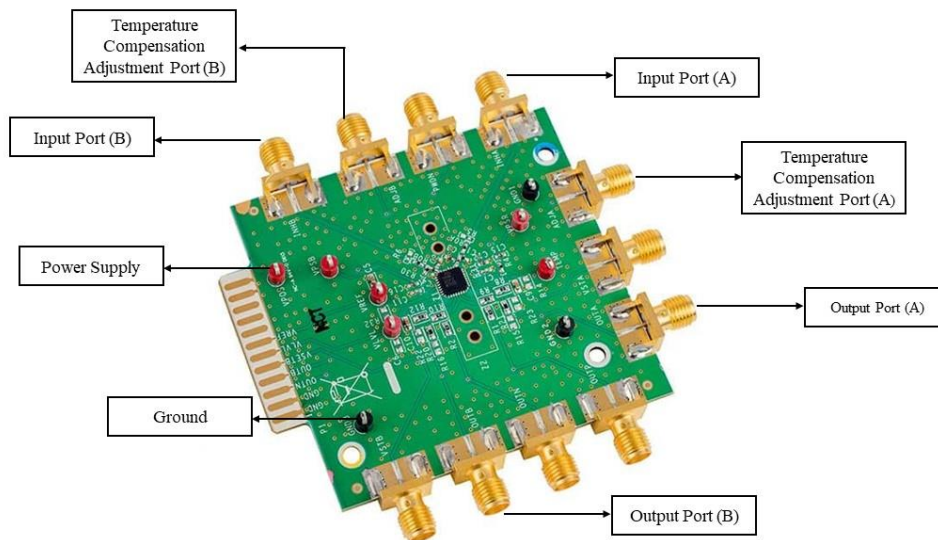
Figure 3.4   View of an ADL5519 RF detector with the indication of the ports used for the portable BMS system [61].

3.3.3 **Signal Generator**

The portable BMS system used the Lab Brick signal generator (LSG-602) from Vaunix Technology, MA USA, as the microwave generator. The LSG-602 is a single port USB Programmable signal generator with a 50 dBm dynamic range. It covers a frequency range from 20 MHz to 6 GHz with maximum output levels of 10 dBm (10 mW) and good spectral purity. There is no requirement for an additional DC power supply to operate the Lab Brick signal generator, and its output includes continuous-wave (CW) and swept-frequency signals. Each device stores settings in internal memory, allowing it to power up in a specific instrument state [62]. The GUI software is installed on an external computer, and the signal generator can be controlled using the Lab Brick library functions and Python pseudocode. The Pseudocode is included in Appendix A.

3.3.4 **Transmitter**

A LB-20200 double-ridged horn antenna, manufactured by ANIFO, China, is used as a transmitter for the portable BMS system. It is rated from 2 GHz to 20 GHz for $|S_{11}|$<-10 dB with an overall gain of 12 dB. The horn antenna is operated in air to reduce losses and limit the mechanical and clinical complications associated with using impedance-matching liquids. The Herrera et al. have shown that commercially available horn antenna (LB-20200) provides better performance in an air medium than custom made Vivaldi and elliptical monopole antennas [63]. Also, LB-20200 exhibits a linear phase delay with distance from the antenna includes an offset $z = p_1 y + p_2$ with $p_1 = 1.18$ and $p_2 = 1.48$ m [63]. The commercial horn antenna is 12.7 cm long, and the aperture has 7.8 cm height and 10.4 cm width.

3.3.5 **Control and Switching Workstation**

The control switching unit synchronizes the microwave signal generation and dc voltage measurements. This module is sectioned into the computer, where the microwave signal generator is connected and controlled, and an Arduino processor controls the switching operation of the system.

a.   **Computer**

The portable BMS system uses a desktop computer. This computer has Windows OS 10 64-bit, Intel (R) Core i5 with 1.60 GHz CPU and 4 GB RAM. USB and LAN cable is used to interface and communicate with the system.

b.   **Arduino Processor**

Arduino is a mini-processor board that uses an ATmega328P microcontroller. The switching workstation has a 16×1 multiplexer, and the Arduino processor controls the multiplexer. The author wrote a program in Arduino Software IDE 1.6 version. The program executes in all Windows operating system by the Arduino Software. During the scan, Arduino produces ON and OFF signal (0 or 1) to control the multiplexer input. Based on the ON/OFF signal, the multiplexer inputs switch one by one for each antenna in the receiver sensor array

for the signal generator's frequency point. The rectification voltage measures using a Keysight Digital Multi-meter and recorded using BenchVue Software for each sensor within the delay period.

3.3.6 Scanning Chamber

The scanning chamber surrounds the object of interest (OI), transmitter horn antenna, and receiver antenna array. It avoids contamination due to noise band mimicking signals from the environment. Figure 3.5 demonstrates the dimension of each wall for the scanning chamber. Three rectangular and semi-circular walls are used to build the scanning chamber. All walls are made with high-density polyethylene plastic to limit unfavorable production of spurious signal and backscattering signals from the environment and the OI, respectively. The chamber is mechanically connected with a servo motor beneath the inspection plate. Rectangular-shaped polyethylene plastic is used to cover the whole BMS system with a 15 cm diameter aperture for the breast. The transmitter horn antenna is supported by a custom-made holder, which is shown in Figure 3.6. The antenna holder hooked up the antenna 11 cm above the inspection plate. It allows modifying the position of the transmitter antenna. The receiver antenna array has been installed on the semi-circular platform.
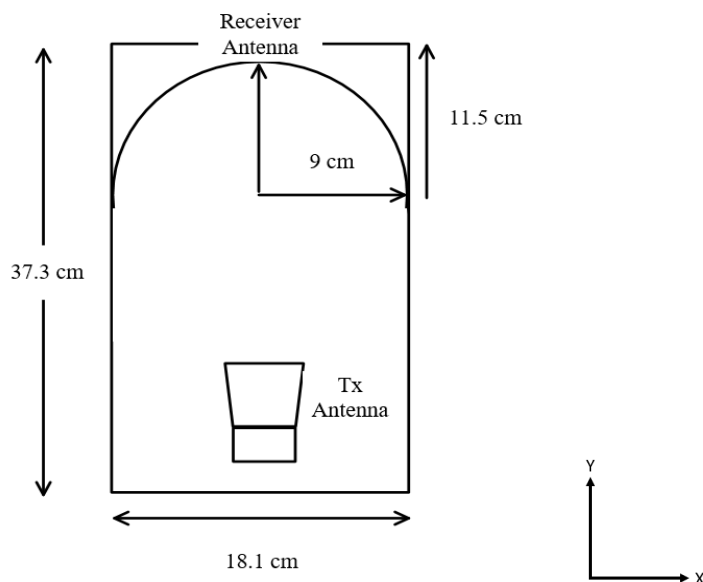
Figure 3.5   Layout of the current scanning chamber of the portable BMS system.
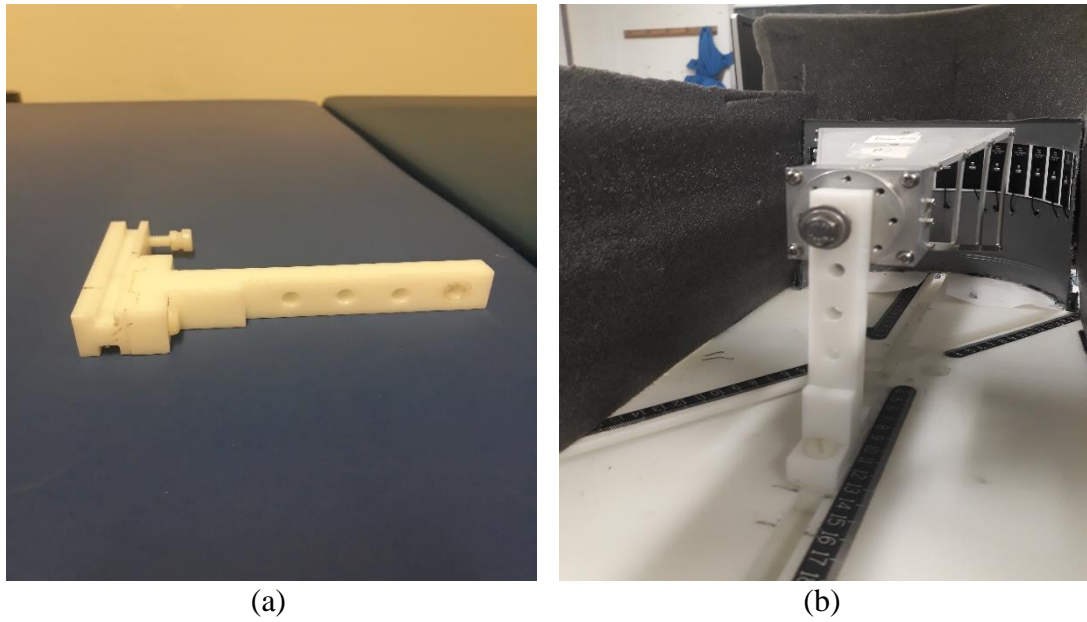
Figure 3.6   Antenna holder for the BMS system with transmitter antenna tilt. a) Single antenna holder at the prone position. (b) Right-angle holder tilt with transmitter antenna.

3.3.7 **Noise Generation**

In the portable system, noise generation occurred due to the electromagnetic interference from the metallic instruments, antenna's cable movement, loose connection, and grounding problems in the circuit. Metallic instruments have scattering properties which interfered with the backscattering electromagnetic waves. For this reason, metallic parts should not be used in the scanning chamber. Antenna's cable movement is associated with spurious electric potential spikes through two different phenomena such as electrostatic discharge and piezoelectricity in the dielectric at microwave frequencies when signals are low [64]. The movement of the dielectric material produces electrostatic discharges in the cable, which affect the scattering parameter in measurement [64]. The cable's deformation can produce electrical potentials due to the piezoelectricity in the dielectric materials of the cable [64]. Less cable movement has been proposed to minimize noise. A loose connection between the receiver antenna and the RF detector can also produce noise. Proper grounding in the switching circuit and the RF detector is necessary to reduce the ripple in the measured voltage.

3.3.8 Single Receiver Antenna Characterization

The usual procedure to test the antenna is to place a known transmitter and the antenna under test, at a known distance. The receiver antenna is working as an antenna under test and testing in an open environment with the help of a known transmitter antenna (horn antenna). The output response of the antenna under test depends on the separation distance (path loss) of the transmitter antenna. The measured amplitude of the signal at the receiver indicates the gain of the antenna under test. The transmitting horn antenna is connected to the signal generator, and the receiver antenna, in the scanning chamber, is placed at 15 cm, 20 cm, and 25 cm from the transmitter (near field regions of horn antenna). The receiver antenna is connected to the RF detector board, which has an inverse relationship with its input power. The RF detector rectified the microwave signal received by the receiver antenna and gave the rectified dc voltage. The rectified dc voltage measures using a Keysight Digital Multi-meter for frequencies from 1.5 to 6 GHz with intervals of 0.1 GHz at constant power (10 dBm) from the signal generator.

3.3.9 Symmetrical Analysis of Left and Right Side Based on the Reference Receiver Antenna

(a)   (b)
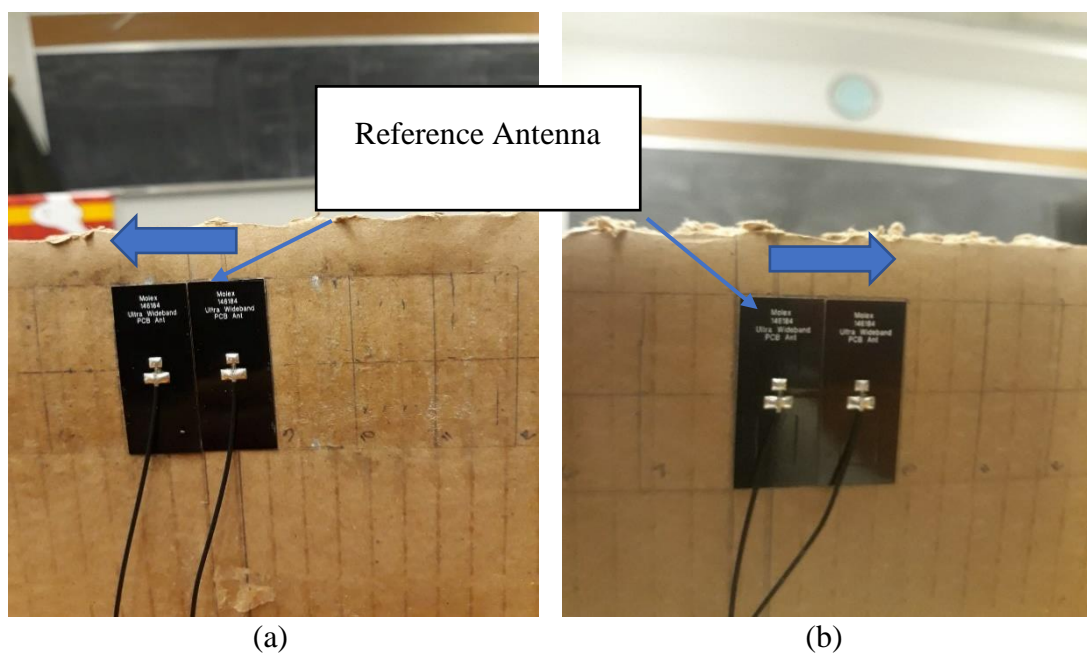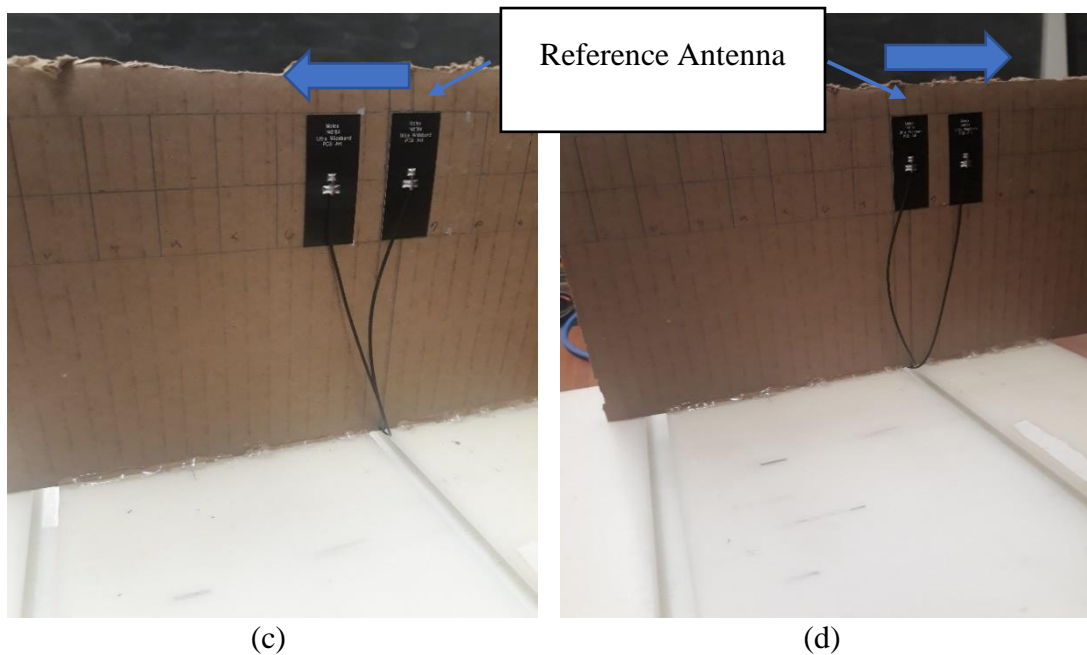
Figure 3.7   The Reference antenna was positioned on the beam axis of the transmitter antenna while the second antenna was placed on the left or right side of the reference antenna. (a), (b) Illustration of zero spacing between two antennas and (c), (d) illustration of antennas with 1 cm spacing between the two antennas.

Symmetrical analysis is one of the fundamental hypotheses to explore and validate of semi-circular model or system [65]. The reference receiver antenna was placed on the beam axis of the transmitting horn antenna with a 20 cm distance. The second receiver antenna placed the immediate left or right side to the reference receiver antenna at 0 cm distance and 1 cm distance between them. The experimental procedure for symmetrical analysis is shown in Figure 3.7.

3.3.10 Mutual Coupling Effect Reduction[1]

Mutual coupling is a common factor in an antenna array design. It modifies the radiation pattern, beam-width, and directivity of an array, and even degrades the performance of adaptive arrays [66]. The optimum nonzero value of mutual coupling will lead to maximum array gain for an antenna array [67]. The Envelope Correlation Coefficient (ECC) defines how

---

[1]Mutual coupling effect reduction (3.3.10) has been reprinted and adapted from the author's paper. Details of the paper are added in the list of achievements section in Appendix E.

the two antennas' radiation patterns are isolated. The ECC is one metric used to determine the effect of mutual coupling in the antenna array [67]. In [68] the author discussed the diversity of mutual coupling between antennas in mobile communication and mentioned that the envelope correlation coefficient should be less than 0.70 at the base station, and less than 0.50 at a the mobile device [68]. The acceptable limit of ECC is less than 0.5 for a UWB-MIMO antenna system [69]. The ECC can be obtained from the scattering (S) parameters for an array of two antennas [69]. Using Scattering parameters, the ECC can be expressed, as shown in equation (3.1), where the $'*'$ symbol represents the complex conjugate of the Scattering parameters. Equation (3.2) is a simplified form of equation (3.1).

$$ECC = \frac{|S_{11}^* S_{12} + S_{21}^* S_{22}|^2}{(1 - |S_{11}|^2 - |S_{21}|^2)(1 - |S_{22}|^2 - |S_{12}|^2)} \tag{3.1}$$

$$ECC = \frac{2Re\{S_{11}S_{21}\}^2}{(1 - |S_{11}|^2 - |S_{21}|^2)(1 - |S_{22}|^2 - |S_{12}|^2)}$$

$$ECC = \frac{4 \times |S_{11}|^2 |S_{21}|^2}{(1 - |S_{11}|^2 - |S_{21}|^2)(1 - |S_{22}|^2 - |S_{12}|^2)} \tag{3.2}$$

To maximize the number of receiver antennas in the array, the optimal spacing between the patch antennas was found by minimizing both the ECC and the antenna spacing.

3.3.11 Time Dependency Test using ANOVA Analysis

The reliability of the portable microwave breast sensing system is defined by its ability to provide constant response over a period without any movement of the cable of the system. The scan was performed under open space conditions on three different days without switching the power supply off. During a scan, there was no cable movement in the system. Table 3.2 summarizes the scan times for different days under open space conditions. A statistical technique was used to compare these three experimental samples and illustrate the variation among and between these samples were from one another. Analysis of variance (ANOVA) is used to analyze the means of different sample groups significantly different from each other. ANOVA estimation procedures that determine the impact of one or more factors by comparing the means of these measured voltages.

Table 3.2   Summarizes the total scan times for three days at open space condition.

Exp. No.	Days	Dates	Time
1	Wednesday to Thursday	20/11/2019 to 21/11/2019	2:00 pm to 1:00 pm
2	Thursday to Friday	21/11/2019 to 22/11/2019	6:00 pm to 5:00 pm
3	Sunday to Monday	24/11/2019 to 25/11/2019	6:00 pm to 1:00 pm

3.3.12 Power Calculation from Simulated E-Field

Assume a lossless antenna is connected to a power source and receives power P from the source at a frequency f. The antenna radiates the power provided by the source. The electromagnetic waves spread to the environment like spheres by increasing radius. The surface of the spheres increases with the square of the distance d from the transmitting antenna. The electromagnetic spheres become a plane wave in far field from the transmitting antenna [70]. Then the power density S (W/m^2) of the plane wave on the receiver antenna at a distance d (m) from the transmitting antenna is stated by the following equation (3.3).

$$S = G_t \frac{P}{4\pi d^2} \tag{3.3}$$

Here, G_t is the gain of transmitting antenna in dB, which can be defined as the ability of the antenna to radiate or concentrate the power in any direction.
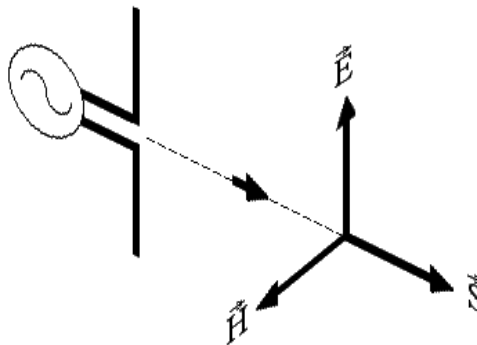
Figure 3.8   Direction of electric (E) and magnetic (H) field for a simple dipole antenna in the far field. Both E and H field are perpendicular to each other. S is also called the Poynting vector.

In Figure 3.8 shows the direction of the electric and magnetic field in the far field region, both are in phase and geometrically perpendicular to each other. The vector S is propagated in the direction of the transverse wave. The electric (E) field depends on the characteristic's impedance of air (Z_0) and magnetic (H) field intensity in the far field region, states by the equation (3.4) considering magnitude. Power density (S) can be expressed in terms of characteristic's impedance (Z_0) and magnetic (H) field intensity in equation (3.5).

$$E = Z_0 H \tag{3.4}$$

$$S = Z_0 H^2 \tag{3.5}$$

From equation 3.3, 3.4 and 3.5,

$$E = \sqrt{\frac{Z_0 G_t}{4\pi d^2}} \sqrt{P} = C\sqrt{P} \tag{3.6}$$

Here, C is defined as a Geometric correlation constant, which depends on the position of the receiver antenna and frequency of the electromagnetic wave. From equation (3.6), it can be concluded that the electric (E) field is proportional to the square root of the power delivered by the transmitter antenna.

3.3.13 **Experimental Setup with a Point Like Scatterer[2]**

The portable BMS system comprises a transmitter horn antenna and an array of 13 ultrawideband balanced microstrip patch antennas, seven radio frequency (RF) detectors, a switching circuit, and the Python-based signal processing. The sensing system, which operates from 1.5 GHz to 6 GHz. The receiver antennas were separated from the transmitting antenna by 20.00 ± 0.05 cm. Seven RF detectors performed the rectification of the received signal. Each RF detector has two (2) channels with a bandwidth of 1 MHz to 10 GHz, and the switching circuit consists of a 16-channel analog multiplexer feeding an Arduino microprocessor. The rectification voltage was measured using a Keysight Digital Multi-meter and recorded using BenchVue Software.

---

[2]Experimental setup with a point like scatterer (3.3.13) has been reprinted and adapted from the author's paper. Details of the paper are included in the list of achievements section in Appendix E
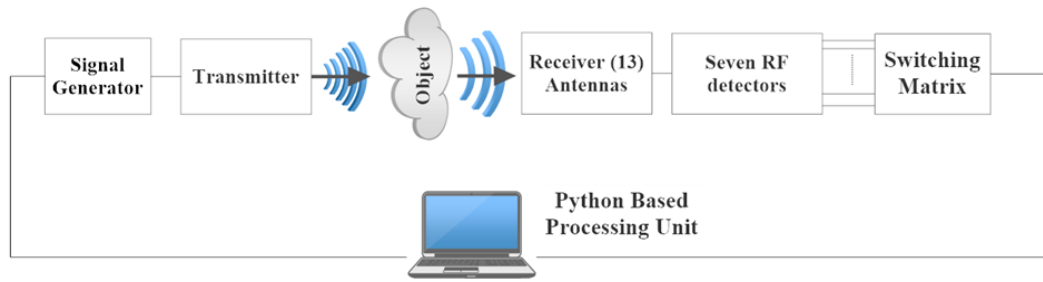
Figure 3.9   The architecture and different components of the proposed experimental portable BMS system.

The proposed microwave sensing system is shown in Figure 3.9. The positions of the antennas in the receiver array system are symmetrical, with antenna 7 lying on the x = 0 axis, and antennas 1 and 13 in the array being symmetrically positioned at y ≈ 0. An aluminum (Al) rod of 6.45 ± 0.05 mm diameter was used to investigate the response of the system to a point-like scatterer as a function of frequency and position. The target of interest was placed at different positions in the scanning plane for frequencies from 1.5 to 6.0 GHz with intervals of 0.5 GHz.

| (a) | (b) |
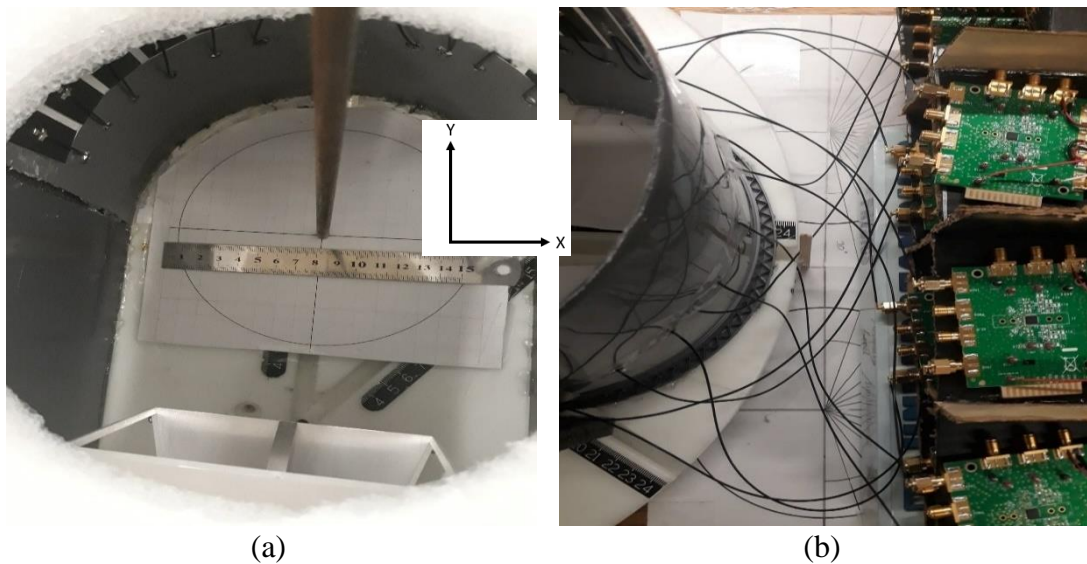
Figure 3.10   (a) Experimental setup with Aluminum (Al) Rod and (b) RF detector connection for the portable system.

3.3.14 Mathematical Modelling of the Portable BMS System

A mathematical model that estimates the microwave power scattered from a point like a scatterer in the portable BMS system under far-field conditions was developed. The general model is formulated as a compact system of rigorous equations. The portable BMS system is made of a complex structure. So, the first step in the modeling was to make some assumptions to simplify the portable BMS system. The model assumes that the microwave transmitter, receiver, and scatterer behave like point sources at their respective positions, as shown in Figure 3.11. The second assumption of the electromagnetic wave propagation analysis is that the scanning chamber's boundary wall does not interrupt the electromagnetic field distribution. The electric field's radiation pattern for each point source assumes the same in the far-field region characteristics.
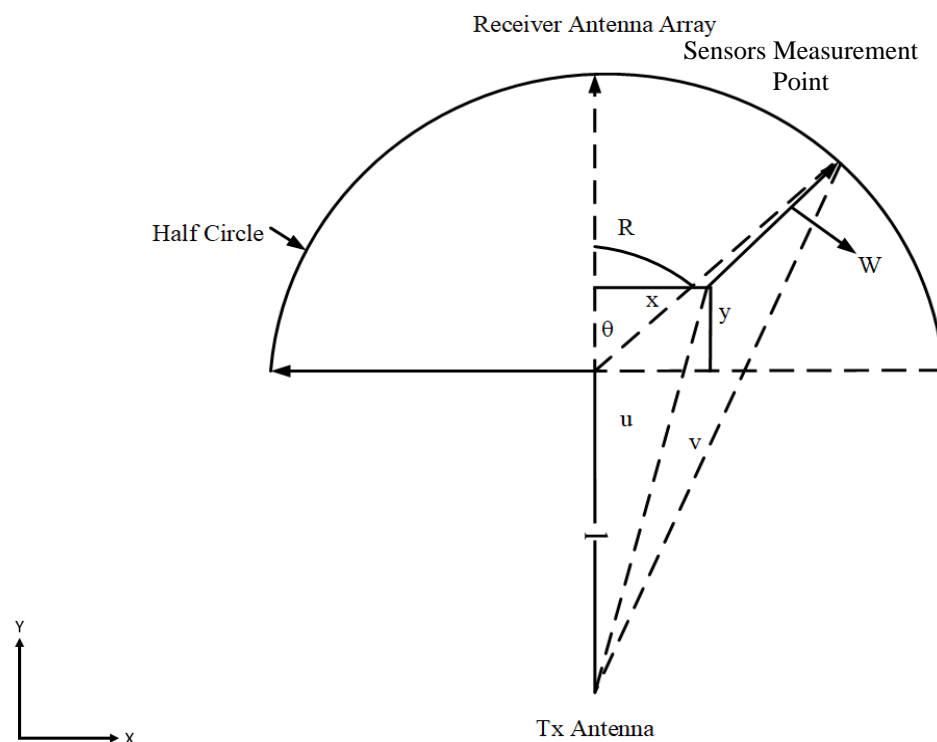
Figure 3.11   Geometrical layout for the experimental setup of the portable BMS system when Al rod placed at (*x, y*) points in the coordinates.

The scatterer is made of homogeneous material, e.g., (Aluminum). The antennas' positions in the receiver sensor array system are symmetrical, with antenna 7 and the transmitter antenna lying on the x = 0 axis. From Figure 3.11, the distance between the transmitter antenna to the sensors and the distance from Al rod to the sensors at the point of

measurement are denoted by v and w, respectively. l is the distance from the transmitter antenna to the center of the coordinates, and the Al rod is placed an arbitrary (x, y) point in those coordinates on the scan plane. u denotes the distance between Al rod to transmitter antenna. The angle is measured between receiver antenna 7 and other positions of the receiver sensor array with respect to the coordinates' center. u, v, and w are the Euclidean distances or norms between different points in the Euclidean space in Figure 3.11, and those distances can be expressed by equations (3.7) to (3.9), respectively. R is the radius of the semicircular platform that holds the receiver antenna array and the distance from the center of coordinates to the sensors at the point of measurement.

$$|u| = \sqrt{(l + y)^2 + x^2} \tag{3.7}$$

$$|v| = \sqrt{(l + R \cos\theta)^2 + (R \sin\theta)^2} \tag{3.8}$$

$$|w| = \sqrt{(R \cos\theta - y)^2 + (R \sin\theta - x)^2} \tag{3.9}$$

Electromagnetic waves travel at the speed of light in a vacuum c with the synchronized propagation of electric and magnetic fields. The polarization of the transmitting horn antenna assumes in the $\hat{z}$ direction. The amplitude of spherical waves in free space (the far-field) depends on $\frac{1}{r}$, where r is the distance in open space from the transmitting horn antenna in the direction of propagation. In practice, the propagation is more complex. The 1/r term falls off as either $1/r^2$ in the transition zone or $1/r^3$ in the Fresnel Zone [70]. However, if the source is extended, as is the case for a point close to a Horn Antenna or an extended rod, the theoretical falloff will be slower [70]. Using the $\lambda/2\pi$ definition for the near-field/far-field boundary [70] , distances of the horn antenna to rod, rod to sensors and antenna to sensors that range from 05 cm to 20 cm, and a bandwidth of 1.5-6.0 GHz, it can be shown that the model needs to work under both the near and far-field conditions. The purpose of this model was to be able to understand the basis for the variation in sensor measurements as a function of the rod position. Thus, to simplify this first order model, the electric field emanating from the transmitter antenna, and from the Rod were expressed using three-dimensional spherical coordinates for far-field approximation as described by equation (3.10).

$$E = \frac{A}{r} \cos\left(\frac{2\pi}{c} fr - 2\pi ft + \emptyset\right) \tag{3.10}$$

where A is the amplitude of the electric field and $\emptyset$ is the phase shift.

The power density S of an electromagnetic wave is proportional to the square of the electric field (E) shown in equation (3.11).

$$S = \varepsilon_0 c E^2 \qquad (3.11)$$

For a continuous sinusoidal electromagnetic wave, the average power density S_{ave} is given by

$$S_{ave} = \langle \varepsilon_0 c E^2 \rangle \qquad (3.12)$$

$$\Rightarrow S_{ave} = \varepsilon_0 c \lim_{T \to \infty} \left(\frac{\int_t^{T+t} A^2 \cos^2 \left(\frac{2\pi}{c} fz - 2\pi ft' + \emptyset \right) dt'}{r^2 T} \right)$$

$$\Rightarrow S_{ave} = \varepsilon_0 c \frac{A^2}{2r^2} \ (\text{W/m}^2) \qquad (3.13)$$

The electric field at the sensors at a distance $|v|$ for open space condition from the transmitter with phase shift $\emptyset$,

$$E_{os} = \frac{A}{v} \cos \left(\frac{2\pi}{c} fv - 2\pi ft + \emptyset \right) \qquad (3.14)$$

The average power density (S_{os}) at the sensors at a distance $|v|$ for open space condition from the transmitter is calculated by

$$S_{os} = \langle \varepsilon_0 c E_{os}^2 \rangle$$

$$\Rightarrow S_{os} = \varepsilon_0 c \lim_{T \to \infty} \left(\frac{\int_t^{T+t} \left(\frac{A}{v} \cos \left(\frac{2\pi}{c} fv - 2\pi ft' + \emptyset \right) \right)^2 dt'}{T} \right)$$

$$\Rightarrow S_{os} = \frac{1}{2} \varepsilon_0 c \frac{A^2}{v^2} \ (\text{W/m}^2) \qquad (3.15)$$

The electric field for Al rod at a distance $|u|$ from the transmitter with phase shift $\emptyset$,

$$E_r = \frac{A}{u} \cos \left(\frac{2\pi}{c} fu - 2\pi ft + \emptyset \right) \qquad (3.16)$$

The average power density (S_r) at Al rod at a distance $|u|$ from the transmitter is calculated by

34

$$S_r = \langle \varepsilon_0 c E_r^2 \rangle$$

$$\Rightarrow S_r = \varepsilon_0 c \lim_{T \to \infty} \left(\frac{\int_t^{T+t} (\frac{A}{u} \cos (\frac{2\pi}{c} fu - 2\pi ft' + \emptyset))^2 \, dt'}{T} \right)$$

$$\Rightarrow S_r = \frac{1}{2} \varepsilon_0 c \frac{A^2}{u^2} \; (\text{W/m}^2) \tag{3.17}$$

The electric field at sensors for Al rod at a distance $|w|$ from receiver sensors at the point of measurement with phase shift φ,

$$E_{rs} = \frac{\frac{1}{2} \varepsilon_0 c \frac{A^2}{u^2}}{w} \cos (\frac{2\pi}{c} fw - 2\pi ft + \varphi) \tag{3.18}$$

When the Al rod is placed at any point in the coordinate system, the sensors receive two microwave signals, one is a direct (open space) microwave signal, and the other is a scattered signal from the Al rod. So, the sum of the electric field at the sensors point of measurement for Al rod in (x, y) point in the coordinates can be expressed by equation (3.19).

$$E_T = E_{os} + E_{rs} \tag{3.19}$$

$$\Rightarrow E_T = \frac{A}{v} \cos \left(\frac{2\pi}{c} fv - 2\pi ft + \emptyset \right) + \frac{\frac{1}{2} \varepsilon_0 c \frac{A^2}{u^2}}{w} \cos (\frac{2\pi}{c} fw - 2\pi ft + \varphi)$$

$$\Rightarrow E_T = \frac{A}{v} \left(\cos (\frac{2\pi}{c} fv - 2\pi ft + \emptyset) + \frac{\varepsilon_0 c A}{2u} \frac{v}{wu} \cos (\frac{2\pi}{c} fw - 2\pi ft + \varphi) \right)$$

$$\Rightarrow E_T = \frac{A}{v} \left(\cos (\frac{2\pi}{c} fv - 2\pi ft + \emptyset) + \frac{\varepsilon_0 c A}{2u\Lambda} \cos (\frac{2\pi}{c} fw - 2\pi ft + \varphi) \right) \tag{3.20}$$

where $\Lambda = \frac{wu}{v}$

The average power density (S_T) for Al rod in (x, y) point in the coordinates can be calculated from equation (3.21)

$$S_T = \langle \varepsilon_0 c E_T^2 \rangle$$

$$= \varepsilon_0 c \lim_{T \to \infty} \left(\frac{\left(\int_t^{T+t} \left(\frac{A}{v} \left(\cos\left(\frac{2\pi}{c} fv - 2\pi ft + \emptyset\right) + \frac{\varepsilon_0 cA}{2u\Lambda} \cos\left(\frac{2\pi}{c} fw - 2\pi ft + \varphi\right) \right) \right)^2 dt' \right)}{T} \right)$$

$$\Rightarrow S_T = \frac{\varepsilon_0 c}{2} \frac{A^2}{v^2} \left(1 + \left(\frac{\varepsilon_0 cA}{2u\Lambda}\right)^2 + \left(\frac{\varepsilon_0 cA}{u\Lambda}\right) \times \cos\left(\frac{2\pi f}{c}(v - w) + (\emptyset - \varphi)\right) \right) \qquad (3.21)$$

The ratio (R) of average power density (S_T) for Al rod in (x, y) point to the average power density (S_{os}) for open space condition at the sensors is expressed by equation (3.22).

$$R = \frac{S_T}{S_{os}} \qquad (3.22)$$

$$\Rightarrow R = 1 + \left(\frac{\varepsilon_0 cA}{2u\Lambda}\right)^2 + \left(\frac{\varepsilon_0 cA}{u\Lambda}\right) \times \cos\left(\frac{2\pi f}{c}(v - w) + (\emptyset - \varphi)\right)$$

$$\Rightarrow R = 1 + \frac{C_1^2}{4u^2\Lambda^2} + \left(\frac{C_1}{u\Lambda}\right) \cos\left(C_2(v - w) + C_3\right) \qquad (3.23)$$

where, $C_1 \alpha \, \varepsilon_0 cA \ (\Omega^{-1})$, $C_2 \alpha \frac{2\pi f}{c} \ (m^{-1})$, $C_3 \alpha \, (\emptyset - \varphi) \ (rad)$

The range of Ratio (R):

When the cosine term = -1,

$$R = 1 + \left(\frac{C_1}{2u\Lambda}\right)^2 - \left(\frac{C_1}{u\Lambda}\right)$$

Possible range of R = [0, ∞)

When the cosine term = 0,

$$R = 1 + \left(\frac{C_1}{2u\Lambda}\right)^2$$

Possible range of R = [1, ∞)

When the cosine term = 1,

$$R = 1 + \left(\frac{C_1}{2u\Lambda}\right)^2 + \left(\frac{C_1}{u\Lambda}\right)$$

Possible range of R = $[0, \infty)$

3.4 Summary

This chapter described the methodology of the portable BMS system development and mathematical model for the portable system. The development procedure of the system was explained. The operations and characteristics of the system each component was detailed. At the end of this chapter, the BMS was represented by a mathematical equation for a point like scatter. The following chapter will present the results and discussion for the experimental work of the portable BMS system.

CHAPTER IV

RESULTS AND DISCUSSIONS

4.1 Introduction

The previous chapter presented the methods and materials for the portable BMS system. The performance of microwave-based sensing systems depends on several factors, including the characterization of sensors, the mutual coupling effect, the gain of each sensor, the

calibration of the sensors, and the agreement between experimental and simulated results. This chapter also explains the time dependency of each sensor based on statistical analysis. Experimental results have been compared to the simulated results for a point like scatterer in the scanning plane. The mathematical modelling results and measured results for the Aluminum (Al) rod in the portable BMS system were compared and are presented in the last section of this chapter.

4.2   Results of Single Receiver Antenna Characterization

The voltage response of a single receiver sensor characterized at three distances (15 cm, 20 cm, and 25 cm) from the transmitter antenna in free space, for frequencies ranging from 1.5 to 6 GHz, is shown in Figure 4.1. Based on the Friis transmission equation for transmitter and receiver antenna, received power decreases with the square of the distance between antennas in the far-field region. However, the three experimental distances are in the near field region, and the relation between received power and the distance between antennas is complex. Nevertheless, the received power decreases with the increase of distance between the transmitter and receiver antenna. The sensor voltages had an inverse trend with the received power. Figure 4.1 illustrates that output voltage increased with the increasing distance between the transmitter and receiver antenna at free space condition, and the receiver antenna's received power decreased.
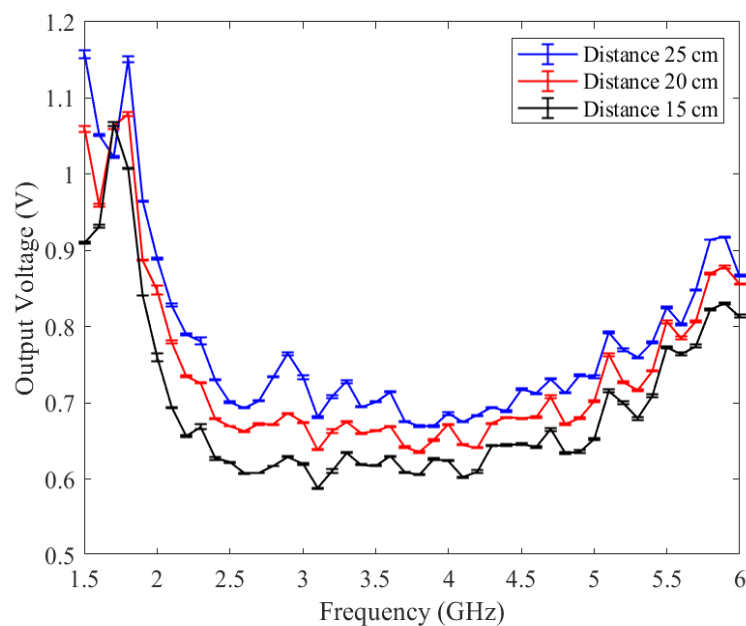
Figure 4.1　　Output voltage characterization for the single receiver (dual-band balanced transmission microstrip patch antenna) antenna for different distances from transmitter horn antenna in free space condition as a function of frequency from 1.5 GHz to 6 GHz.

4.3　Results of Symmetrical Analysis of Left and Right Side Based on the Reference Antenna

Figure 4.2 shows the antenna's response for the symmetrical position with respect to the reference antenna, which was directly in line on the beam axis with the transmitter horn antenna. There was 0 cm distance between the reference antenna and the receiver antenna immediately to its left or right. For this analysis, the experimental setup described in Section 3.3.9 was used. The reference antenna had similar responses for the left or right antenna presence to it, as shown by the dashed line in Figure 4.2 (a). As symmetrical (left and right) position antenna had equal distance from the transmitter horn antenna, they received the same power from the transmitter antenna. Both antennas have a symmetrical response for frequencies from 1.5 to 6 GHz frequency. Figure. 4.2 (b) shows the normal distribution of the percentage of response differences for the left and right antenna from 1.5 to 6 GHz frequency. The difference at 95% of the expected population ($\bar{x} \pm 2\sigma$) ranged from -1.42% to 1.85%.

(a)　　　　　　　　　　　　　(b)
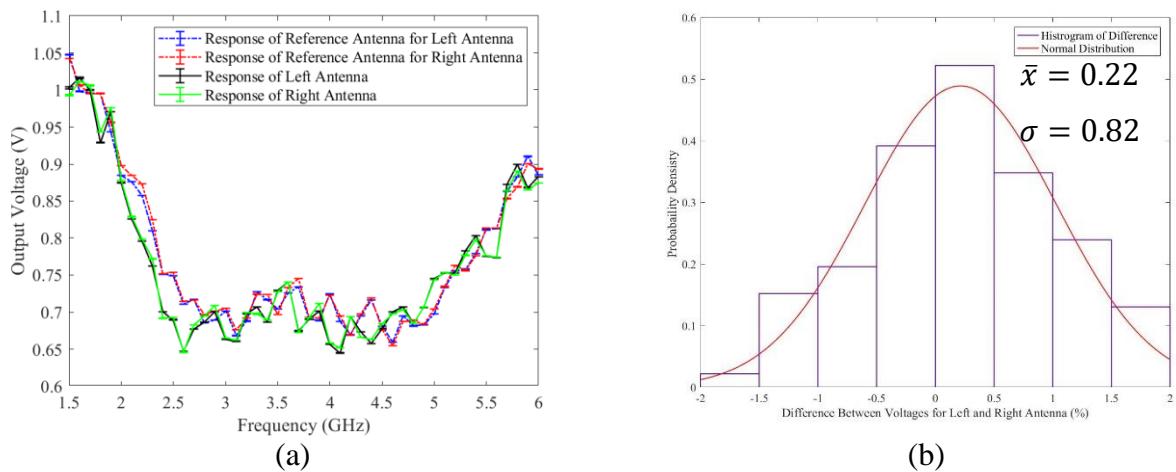
Figure 4.2　　(a) Solid (black and green colour) lines represent output voltage comparison between left and right antennas when two antennas had 0 cm distance and dash (blue and red colour) lines represent the reference antenna's response for left and right antenna. (b) A histogram of the percentage of differences between the output voltage for left and right antennas from 1.5 GHz to 6 GHz was fitted with a normal distribution.

39

(a)   (b)
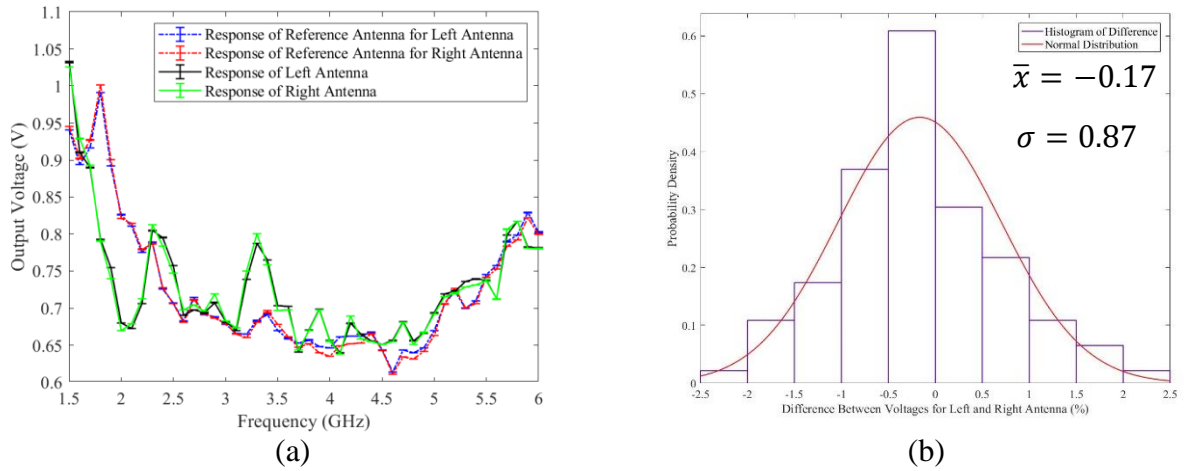
Figure 4.3   (a) Solid (black and green colour) lines represent output voltage comparison between left and right antennas when two antennas had 1 cm distance and dash (blue and red colour) lines represent the reference antenna's response for left and right antenna. (b) A histogram of the percentage of differences between the output voltage for left and right antennas from 1.5 GHz to 6 GHz was fitted with a normal distribution.

Figure 4.3 represents similar experimental results for 1 cm distance from the reference antenna to its immediate left or right antenna in the receiver. The percentage differences in the responses for the left and right antennas for frequencies from 1.5 GHz to 6 GHz varied from -1.90 % to 1.57% at the 95% confidence interval.

4.4   Results of Mutual Coupling Effect on Reflection Coefficients

R.P. Jedlicka et al. [71] concluded that separation between antenna element has a monotonical effect on the mutual coupling level, and it decreases with increased separation gap between antennas. The solid black line in Figure 4.4 represents the measured reflection coefficient for the reference antenna when it is alone in the receiver array. There was 0 cm horizontal separation between each antenna in the receiver array. The reflection coefficient (S_{11}) for the reference antenna was increased with the consecutive addition of an antenna to the immediate left and right side of the reference antenna in the array. The increase in the reflection coefficient was due to an increase in mutual coupling. Then, the reference antenna's reflection coefficient maintained a constant pattern after the addition of the other's antenna in the array.

40

The solid blue line shows the difference of reflection coefficient between the single reference antenna and the reference antenna with a first left antenna to it in Figure 4.5. The reference antenna had mutual coupling for its first left and right antenna.
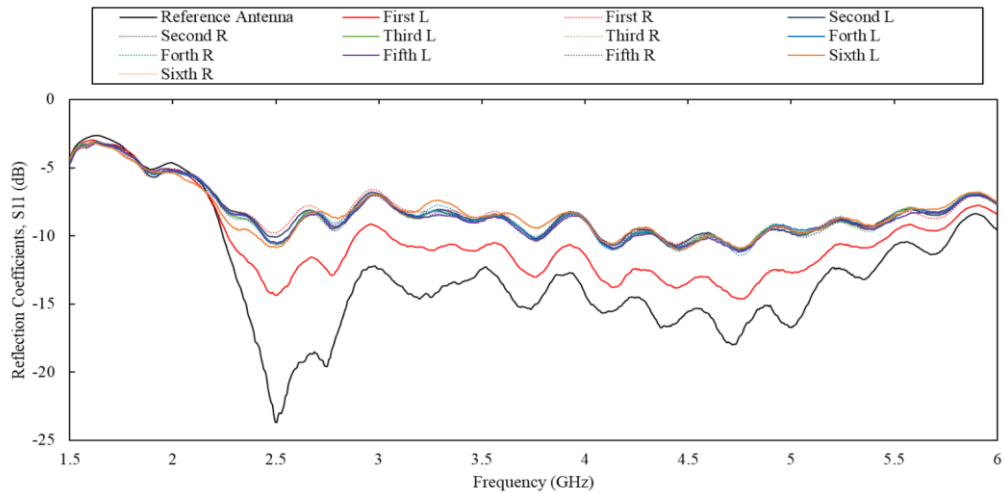
Figure 4.4   Measured Reflection coefficients (S_{11}) for the reference antenna when it was single in the array and consecutively added the other antennas to the reference antenna's left and right side. Due to mutual coupling, the reflection coefficient increased for the reference antenna in the receiver array.
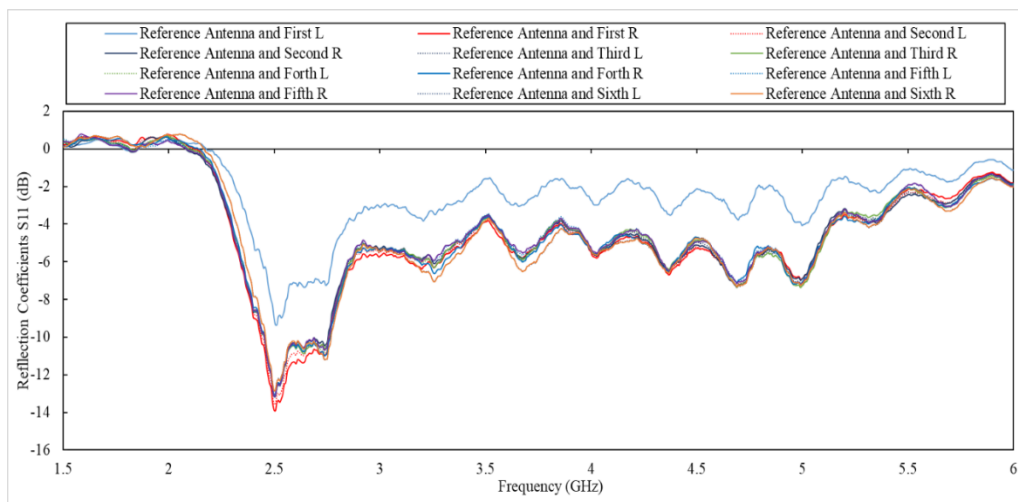
Figure 4.5   The difference between the measured reflection coefficient (S_{11}) for the reference antenna when the reference antenna was single in the array and the other antennas consecutively added in the array to the left and right side of the reference antenna.

4.5   Calculation of Optimal Separation of Antennas in Receiver Array

The calculated Envelope Correlation Coefficient (ECC) for different horizontal separation distances between two receiver antennas is shown in Figure 4.6. The calculated ECC decreased with the increasing separation distance, and a maximum ECC occurred when there was no separation between two receiver antennas. The normalized maximum ECC for separation distances of 0 to 15 mm is shown in Figure 4.7 (a). Since the ideal sensor array would have zero spacing and an ECC = 0, the optimal spacing was obtained by selecting a spacing that minimized both ECC and spacing using the shortest distance to (ECC = 0, NDD = 0) as illustrated in Figure 4.7 (a). At this point, the calculated ECC was 0.37, which is less than the recommended constraint of 0.50 for the UWB-MIMO antenna system, and the optimal horizontal separation between each antenna in the receiver array was 4 mm. The number of antennas in the receiver array decreased with the increasing function of antenna spacing, as shown in Figure 4.7 (b). A maximum of 16 antennas could be placed on the semicircular platform with 0 mm spacing. But at 0 mm spacing, the ECC was 0.99. At 3 mm antenna spacing, 14 antennas could be accommodated with a max ECC of 0.47. In order to include a reference antenna on the beam axis of the transmitter horn antenna, an odd number of antennas was preferred. With 4 mm antenna spacing, the maximum ECC was 0.37, and this value was less than 0.50 with 13 antennas in the array. This 4 mm spacing was deemed to be a reasonable trade-off between maximizing the number of antennas in the receiver array and minimizing of the ECC.
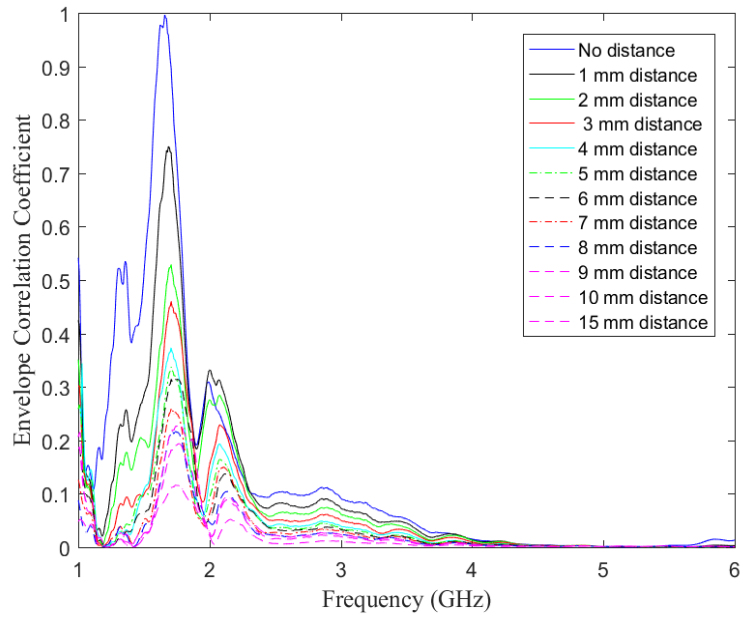
Figure 4.6   The Envelope Correlation Coefficient (ECC) as a function of frequency for horizontal separation distances from 0 to 15 mm between two receiver antennas.

(a)

(b)
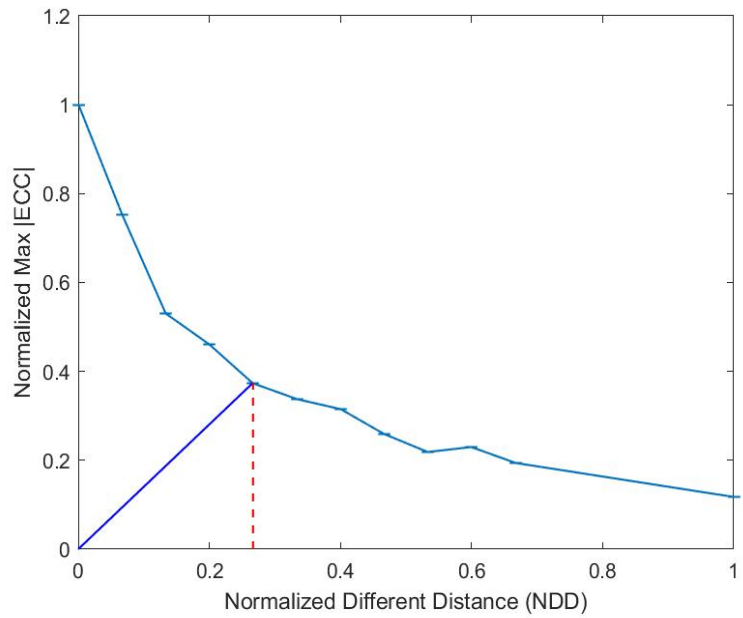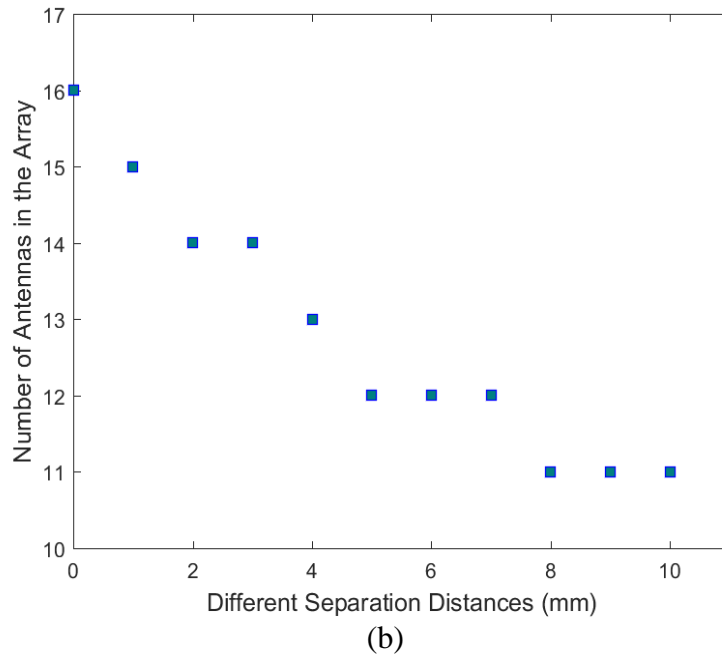
Figure 4.7   (a) Output from the parametric study of the Envelope Correlation Coefficient (ECC), normalized to the maximum ECC value of 0.99, for distances from 0 to 15 mm between two receiver antennas, normalized to the maximum 15 mm spacing (NDD). (b) Number of antennas in the receiver antenna array as a function of different separation distances from 0 mm to 10 mm.
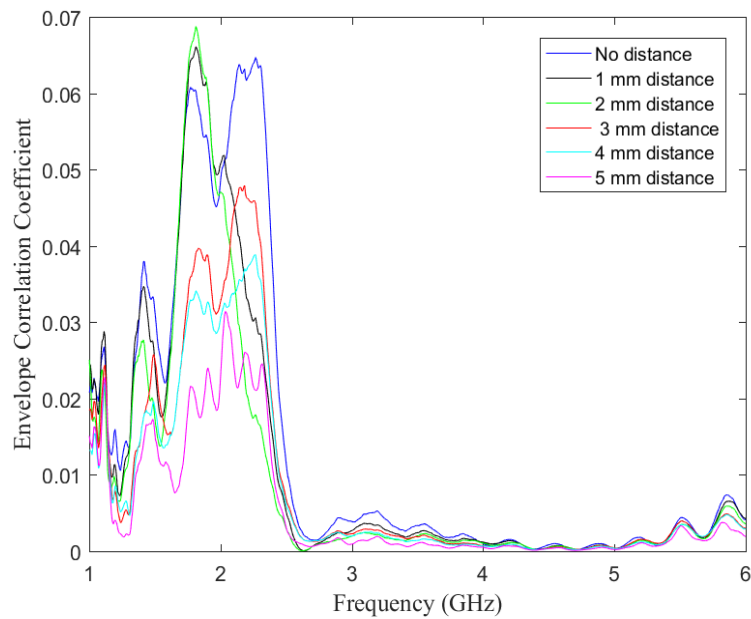
Figure 4.8   The Envelope Correlation Coefficient (ECC) as a function of frequency for vertical separation distances from 0 to 5 mm between two receiver antennas.

Figure 4.8 illustrates the calculated ECC for different vertical separation distances between two receiver antennas. The maximum ECC for vertical separation was less than 0.07, which is below the recommended constraint of 0.50. The optimal vertical separation between two receiver antennas in the receiver array was 0 mm distance with 180-degree vertical orientation.

4.6 Number of Antenna Calculation in Receiver Array

Figure 4.9 illustrates that the number of antennas (N) in the receiver array depends on the arc length of the half-circle (s), the width of a single microstrip patch antenna (W=17.4 mm) and the optimal separation of antennas in the receiver array, which in this case is 4 mm.
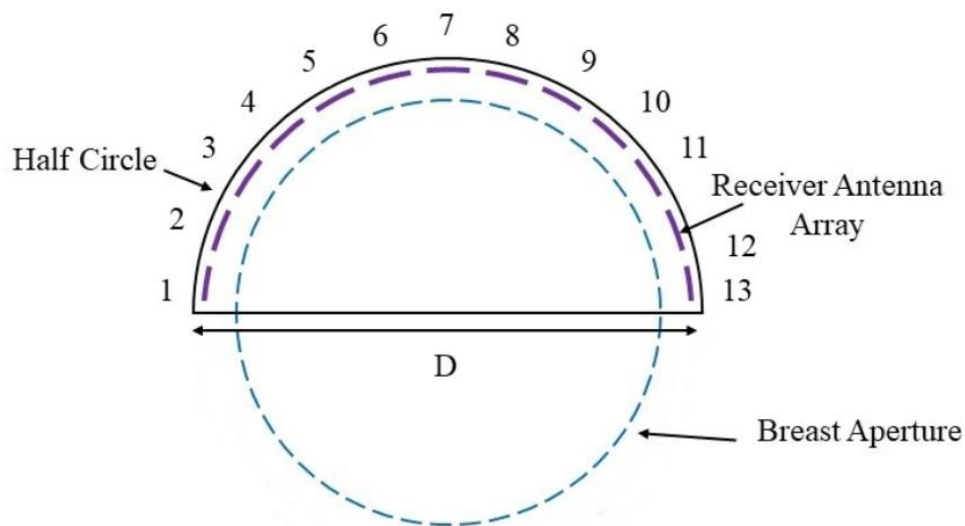
Figure 4.9   Illustration of the receiver array of microstrip patch antennas surrounding a circular breast aperture. The configuration resembles the shape of a half-circle with diameter D. The width of the single microstrip patch antenna is 17.4 mm.

Arc length of half-circle,

$$s = \pi \times \frac{D}{2} = \pi \times 90 \cong 282.7 \text{ mm}$$

The number of antennas in receiver array,

$$N = \frac{S}{W+4} = \frac{S}{17.4+4} \cong 13$$

In the receiver antenna array, one receiver antenna was placed directly inline on the beam axis with the transmitter horn antenna. Six antennas were placed on the right side, and the other six antennas were placed on the left side to the central receiver antenna.

4.7 Results of Time Dependency Test

The bar diagram illustrated in figure 4.10 shows the probability value (p value) from a one-way ANOVA analysis for three days voltage measurements of 13 antennas at 2.5 GHz frequency. A test of equality variance was carried out at the 95% CI showed that the variance was not equal. A one-way ANOVA for non-equal variance at 95% confidence interval using Welch's test was carried out, which shows strong evidence for the null hypothesis (p value > 0.05), which means that the variations for three days were not significantly different for 13 antennas. This implies that each antenna in the receiver array had a constant output voltage with respect to time if there was no cable or mechanical setup movement.
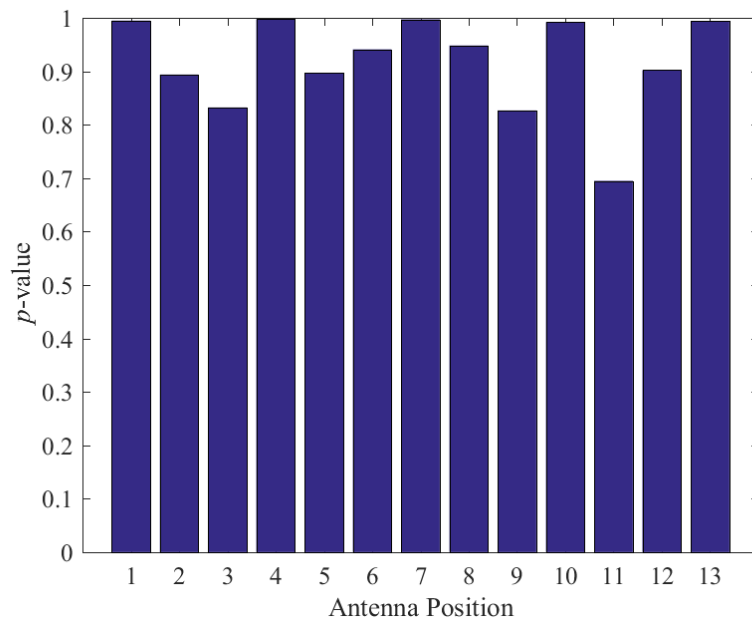
Figure 4.10   A bar diagram of the p value from one-way ANOVA analysis at 95% confidence interval for 13 antennas for three days measurement at 2.5 GHz frequency.

4.8   Calibration of the Portable System

The portable BMS system was designed in Computer Simulation Technology (CST) Microwave Studio to mimic the experimental setup. The calibration of the portable BMS system was carried out using the E-field generated from CST simulation for the breast scanning chamber in air (open chamber) and when a point like scatterer (Al rod) was presented in the breast scanning chamber. Figure 4.11 shows the simulated magnitude of the E-fields for open space conditions at 2.5 GHz and 4 GHz frequencies at the 13 antenna positions and the measured voltage from the sensors connected to those antennas. The antennas' positions in the receiver array system are symmetrical, with antenna 7 lying on the x = 0 axis, and antennas 1 and 13 in the array being symmetrically positioned at y ≈ 0. The E-field distributions from CST simulation were symmetrical. Likewise, the measured open space sensor voltages were symmetrical.

(a)   (b)
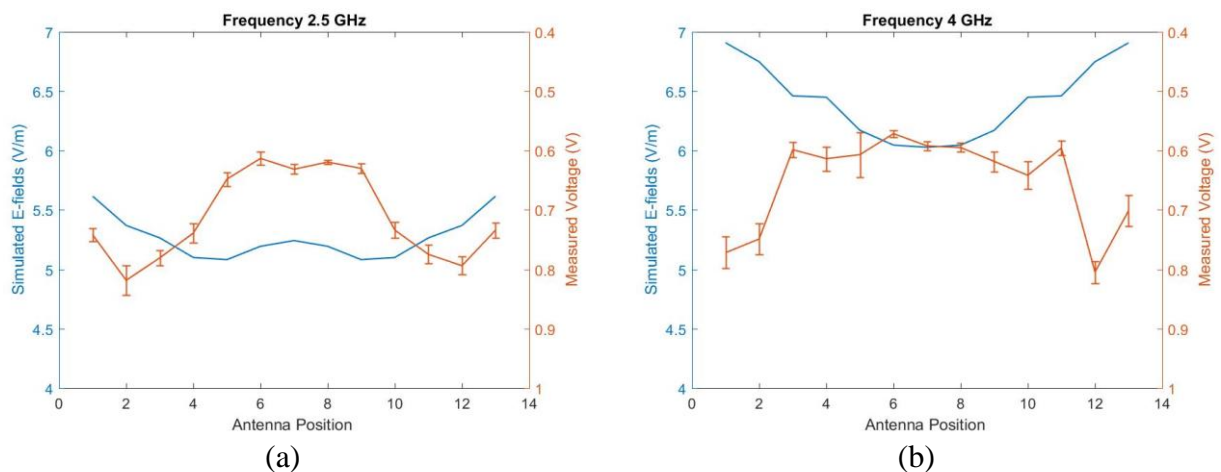
Figure 4.11   Simulated E-fields and measured voltage patterns for open space conditions at frequencies of (a) 2.5 GHz and (b) 4 GHz. The simulated E-field distributions and the measured voltages were symmetrical in the semicircular receiver array.

The open space measured output voltage had a linear relationship to the input power given by equation (4.1), with some typical parameters and correlation coefficients shown in Table 1 for antennas 1 and 13 at 2.5 GHz and 4.0 GHz. The linear parameters (*A*, *B*) table can be found in Appendix B for 13 receiver antenna and 10 frequency points. While the gain or

weight factors of each symmetrically positioned antenna were approximately equal, the bias factors at 0 dBm input power, shown in Figure 4.12 (a), were different.

$$V(voltage) = (B \pm \Delta B) + (A \pm \Delta A) \times P(Power, dBm) \qquad (4.1)$$

Table 4.1　　　　Linear parameters with two standard deviation and correlation coefficients for antennas 1 and 13 at 2.5 GHz and 4 GHz.

Frequency (GHz)	Antenna Number	Gain or Weight Factor, A (dBm/Volts)	Bias Factor, B (Volts)	correlation coefficient	RMSE
2.5	1	-0.0226 ± 0.0002	0.956 ± 0.004	0.9998	0.0044
	13	-0.0219 ± 0.0006	0.935 ± 0.008		
4	1	-0.0229 ± 0.0014	0.999 ± 0.014	0.9998	0.0046
	13	-0.0226 ± 0.0026	0.929 ± 0.031		
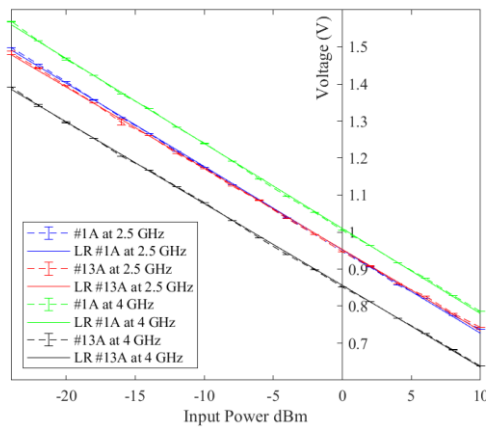
(a)
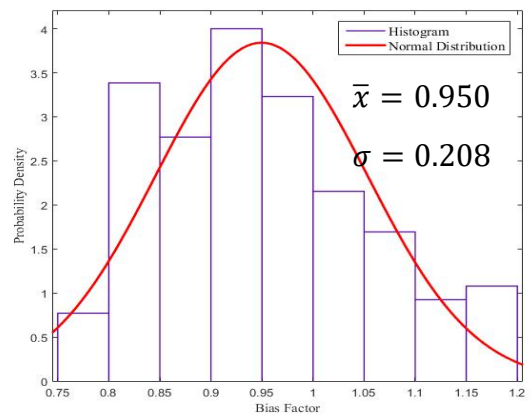
(b)

Figure 4.12　　(a) The dashed lines represent the measured voltage, while the solid lines represent the corresponding regression line for antenna number 1 and 13 with respect to different input power (dBm) at 2.5 GHz and 4 GHz. Each symmetrical sensor has approximately the same gain or weight factor but different bias factors at 0 dBm input power. (b) The bias factor distribution for 13 antennas and 10 frequency points from 1.5 GHz to 6 GHz, stepped at intervals of 0.5 GHz.

According to the linear relationship, all sensors had a negative gain or weight factor ranging from -0.0230 dBm/V to -0.0210 dBm/V with a mean and two standard deviations of -0.0219 ± 0.0007 dBm/V. Figure. 4.12 (b) shows the probability distribution of the bias factor for all antennas at ten frequency points. The bias factor for 95% of the expected population

$(\bar{x} \pm 2\sigma)$, ranged from 0.752 V to 1.167 V. As described in 3.3.12, from the approximation of far-field antenna behaviour, the electric field strength E depends on the square root of input power in watts in the following equation (4.2). Where the electric field strength E (V/m), geometric correction constant C, and input power P (W). Geometric correlation constant, C is an array, which varies for 13 receiver antennas (Ant), and ten frequency points (F) from 1.5 to 6 GHz with intervals of 0.5 GHz.

$$C(Ant, F) = \frac{\sqrt{P}}{E(Ant, F)} \tag{4.2}$$
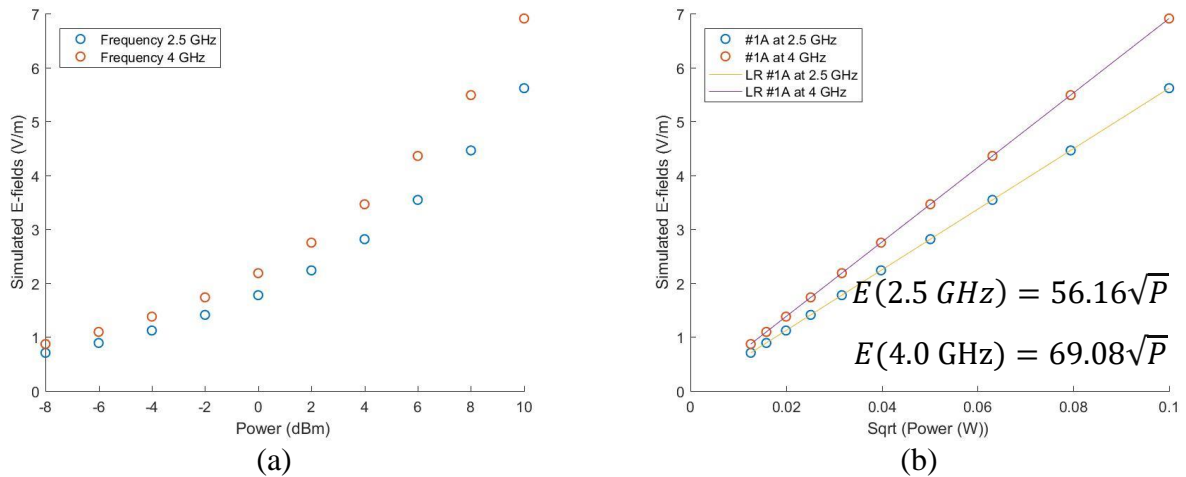
Figure 4.13   Simulated E-fields with respect to input power (dBm) for frequencies of (a) 2.5 GHz, and (b) 4 GHz. Simulated E-fields had an exponential relationship with input power (dBm). E-fields had a linear relationship with the square root of input power (W).

The relationship of the E-field with respect to input power is shown in Figure 4.13. Figure 4.13 illustrates that E-field exponentially increased as a function of the input power (dBm) and had linear behaviour with the square root of power (W) at 2.5 GHz and 4 GHz frequency for antenna number one in the receiver array. A geometric constant was calculated using the simulated E-field (E) in the receiver array and the transmitted power (P). A table of the geometric correlation constants C is given in Appendix C for 13 receiver antenna and 10 frequency points.

$$Calculated\ Voltage\ (Vc) = C \times Simulated\ Power\ (Ps) \tag{4.3}$$

Based on the geometric correlation constants, simulated power (P_s) was derived from the simulated E-field at the receiver antennas. A 13×10 array of calibration constants was determined from the simulated power and the measured voltage from the equation 4.3. A table of the calibration constants $\mathbb{C}$ is given in Appendix D for 13 receiver antenna and 10 frequency points. The measured and calculated voltages agreed with each other after open space calibration for 2.5 and 4.0 GHz frequency as shown in Figure 4.14. The measured and calculated voltages had a good agreement after open space calibration. These open space calibration constants were used for further calibration with the point like scatterer in the scanning chamber.
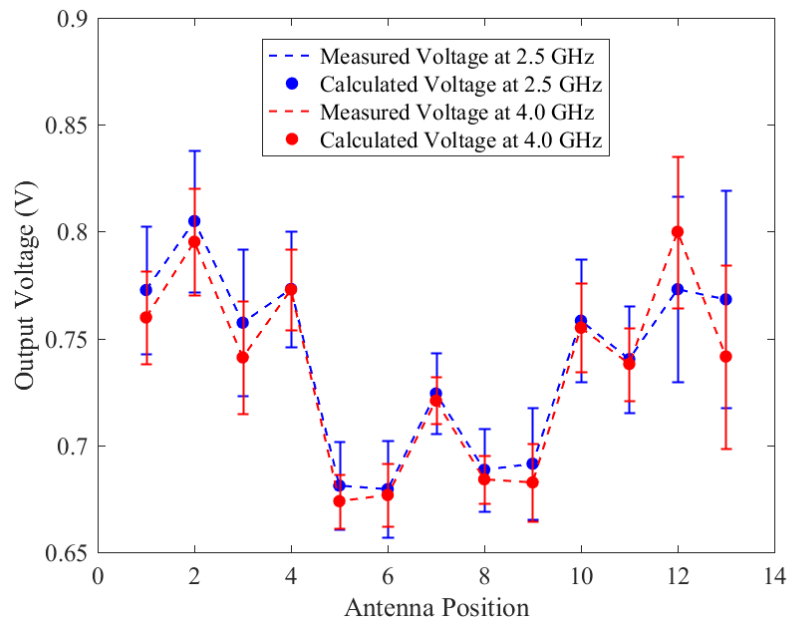
Figure 4.14   Dashed (blue and red) lines represent measured voltages and scatter (blue and red) plots represent calculated voltages from simulated E-field at receiver antennas and calibration constant for open space condition at frequencies of 2.5 GHz and 4.0 GHz.

Figure 4.15 (a) illustrates the measured and calculated voltages from the simulated E-field for the Aluminum (Al) rod at point (-6 cm, 0 cm) at frequencies of 2.5 GHz and 4 GHz. The measured and calculated voltages for all receiver antennas were not equal because of slight differences in the experimental setup and simulation environment. Figure 4.15 (b) shows the percentage distribution of the differences between the calculated and measured voltages for the three rod positions (-6 cm, 0 cm), (0 cm, 0 cm) and (6 cm, 0 cm). The error distributions were normally distributed. A one-way ANOVA for non-equal variance using Welch's test showed

(a)

$$\bar{x} = -1.06$$

$$\sigma = 7.17$$

(b)
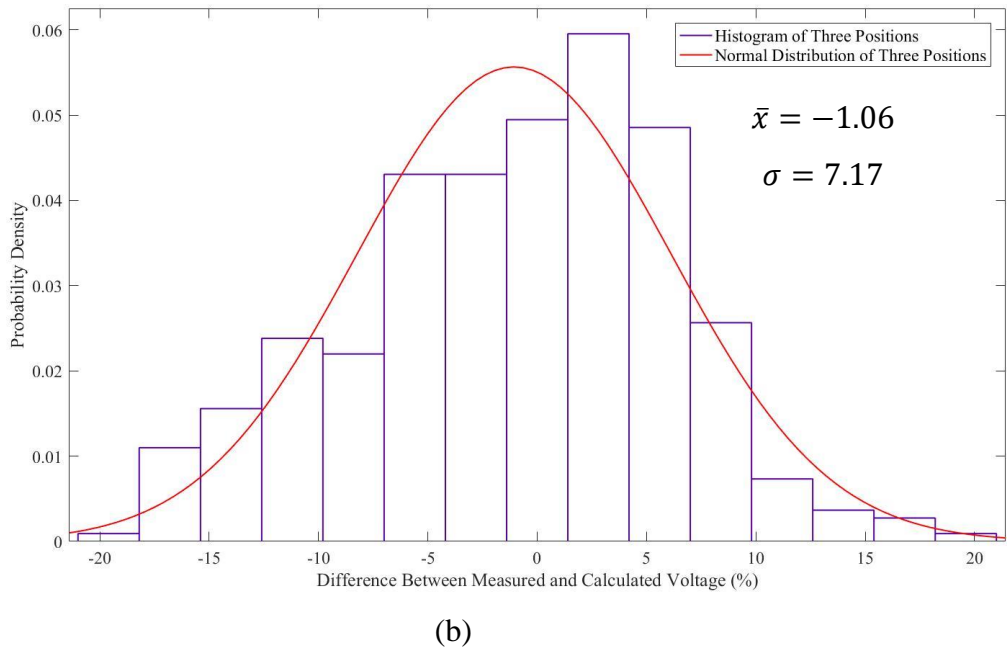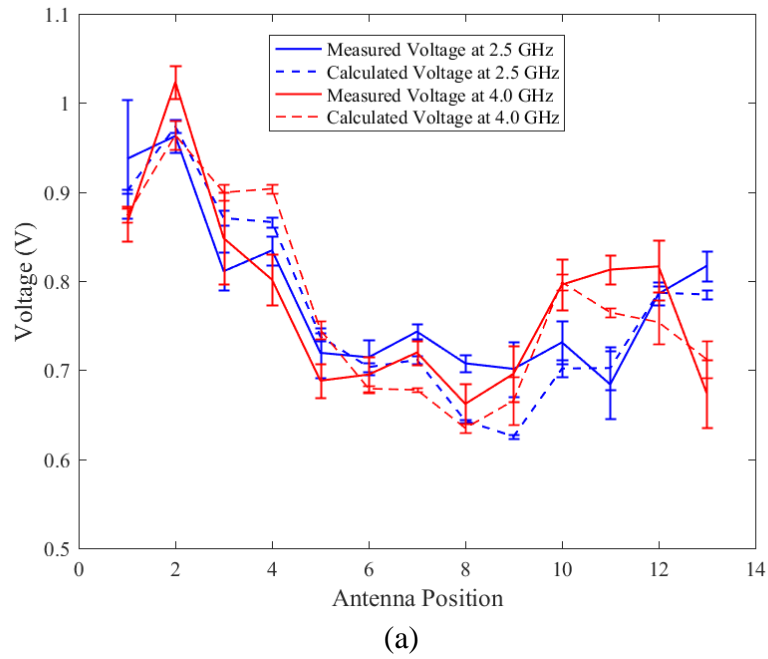
Figure 4.15   (a) Solid (blue and red) lines represent the measured voltage and dashed (blue and red) lines represent the calculated voltage from simulated E-field patterns for the Aluminum (Al) rod at point (-6 cm, 0 cm), and 2.5 GHz and 4 GHz frequencies. (b) A histogram of the percentage differences between the calculated and experimental voltage for an Al rod at three positions (-6 cm, 0 cm), (0 cm, 0 cm), (6 cm, 0 cm) for 13 antennas and 10 frequency points from 1.5 GHz to 6 GHz, stepped at intervals of 0.5 GHz, fitted with a normal distribution.

strong evidence for the null hypothesis ($p = 0.95 > 0.05$), which concludes that the mean differences for the three different rod positions were not significant. The differences in the measured and calculated voltages for receiver antennas from 1.5 GHz to 6 GHz were approximately ± 15% at the 95% confidence interval.

4.9   Comparison of the Experimental and Simulated Power Measurements for Open Space Conditions

Figure 4.16 (a) represents the normal distribution for 130 sample points of the measured power in the 13 antennas and 10 frequency points for open space measurement. The receiver antenna array's measured power ranged from 10.3 dBm to 9.3 dBm with a mean ± SD of 9.8 dBm ± 0.3 dBm at the 95% confidence interval. However, cable movement produced uncertainty in the experimental work. Measured power was approximately similar to the symmetrical antenna position within the uncertainties. In the simulated environment, there was no cable or positional movement of the transmitter and receiver so, the received power was 10 dBm. The percentage difference between simulated and measured power ranged from -3.4% to 7.9%, as shown in Figure 4.16 (b).

(a)   (b)
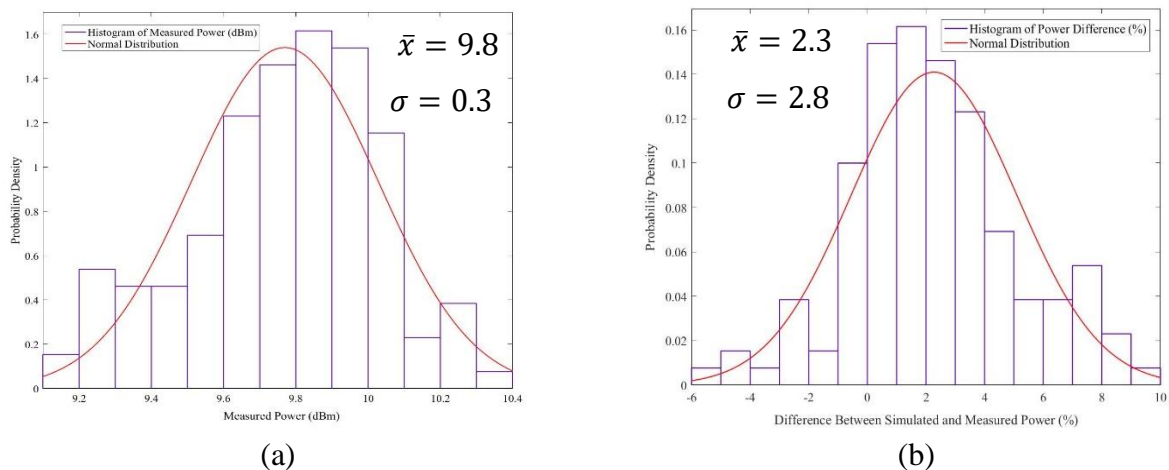
Figure 4.16   (a) A histogram of the measured power in the receiver antenna array from 1.5 GHz to 6 GHz, stepped with intervals of 0.5 GHz, fitted with a normal distribution. (b)The distribution of the percentage difference between the simulated and experimental power for 13 antennas with 10 frequency points from 1.5 GHz to 6 GHz stepped with intervals of 0.5 GHz.

4.10 Comparison of Experimental and Simulated Power Measurements for a Point Like Scatterer

The relative power (RP) is the ratio of the received power at the receiver array for the Al rod at the different position in the scanning plane, compared with open space received power at the receiver array expressed by equation (4.3).

$$Relative\ Power\ (RP) = \frac{\begin{array}{c}Measured\ power\ for\ the\ scatterer\ at\\ different\ position\ in\ the\ scanning\ plane\end{array}}{Measured\ power\ at\ open\ space\ condition} \tag{4.4}$$

The relative power at the receiver antenna array shown in Figure 4.17 followed the additive and subtractive properties of the transmitted and scattered signals for different Al rod positions. Figure 4.17 (a)-(d) represents the relative power with respect to the open space simulated power at the receiver array for the Al rod on the X-axis (i.e., Y is zero) of the scanning grid from X = -6 cm to X = 6 cm with intervals of 2 cm. The solid (red and blue colour) lines represent simulated relative power at 2.5 GHz. For the simulated data, the relative powers were equal for symmetrically positioned antennas for symmetrical positions of the Al rod in the scanning plane. For example, the relative power at antenna 1 when the Al rod was at the (-6, 0) position was the same as the relative power at antenna 13 for the Al rod (6, 0) position. Figure 4.17 also illustrates that the relative power at antenna 1 and antenna 13 were equal for the Al rod at the (0, 0) position.
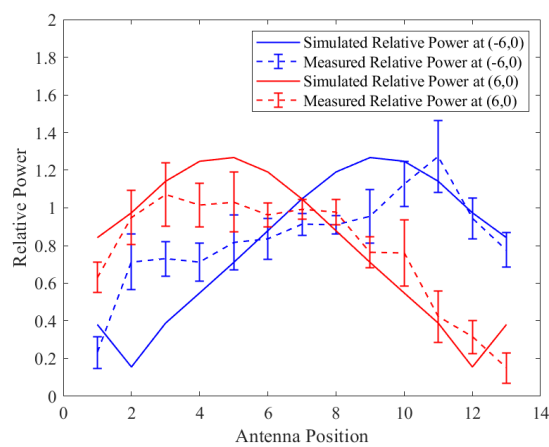
(a)
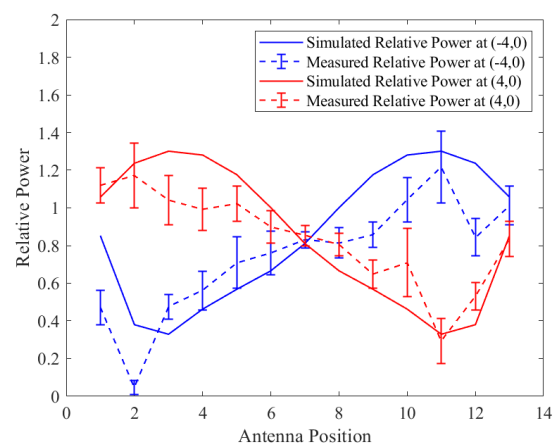
(b)
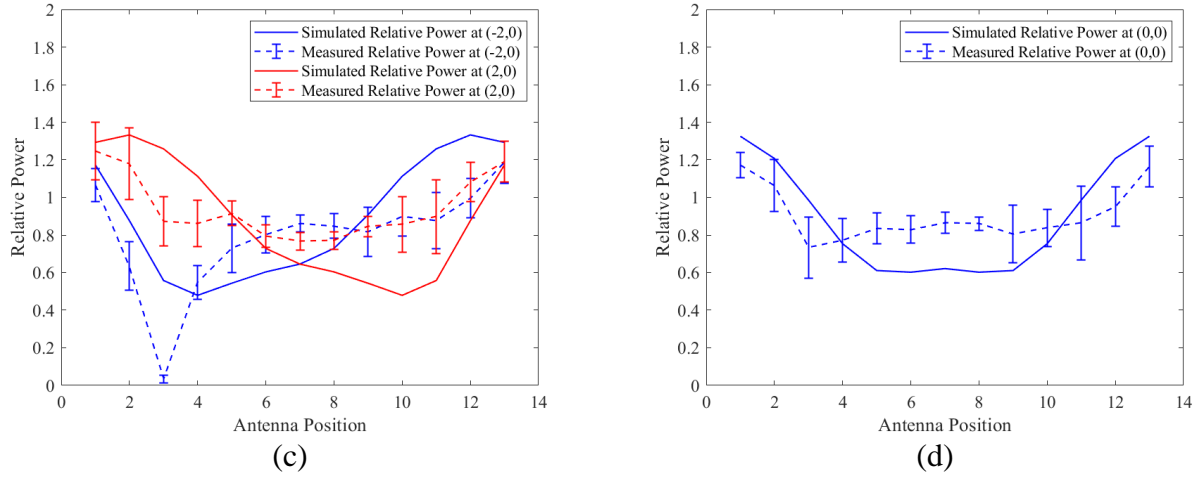
Figure 4.17   (a)-(d) Relative power (RP) for the Al rod in the scan plane at (-6,0) and (6,0), (-4,0) and (4,0), (-2,0) and (2,0), (0,0), with respect to the power at open space in the receiver array for measured and simulated results at 2.5 GHz.

The dashed (red and blue colour) lines represent the measured relative power at 2.5 GHz frequency. For the measured data, the relative powers followed approximately symmetric trends but were not equal for the symmetrical position antennas at the symmetrical position of the Al rod in the scanning plane. This is possibly as a result of errors in the mechanical setup, where, unlike the simulation environment, it was more difficult to precisely position the Al rod. The average relative power (ARP) defines as the average between the relative power of the symmetrical antenna position in the receiver array at the symmetrical Al rod in the scanning plane expressed in equation (4.4).

$$Average\ Relative\ Power\ (ARP) = \frac{RP\ for\ antenna\ 1\ at\ (-6,0) + RP\ for\ antenna\ 13\ at\ (6,0)}{2} \quad (4.5)$$

In Figure 4.18, the dashed line represents the measured ARP, and the solid line represents the simulated ARP. While there are similar trends, the measured and simulated ARP in the receiver array were not in agreement. The scatter plot in Figure 4.18 represents the difference between measured and simulated ARP at 2.5 GHz. The difference of ARP was varied from -0.40 to 0.35 at the 95% Confidence Interval over the 13 antennas in the receiver array.
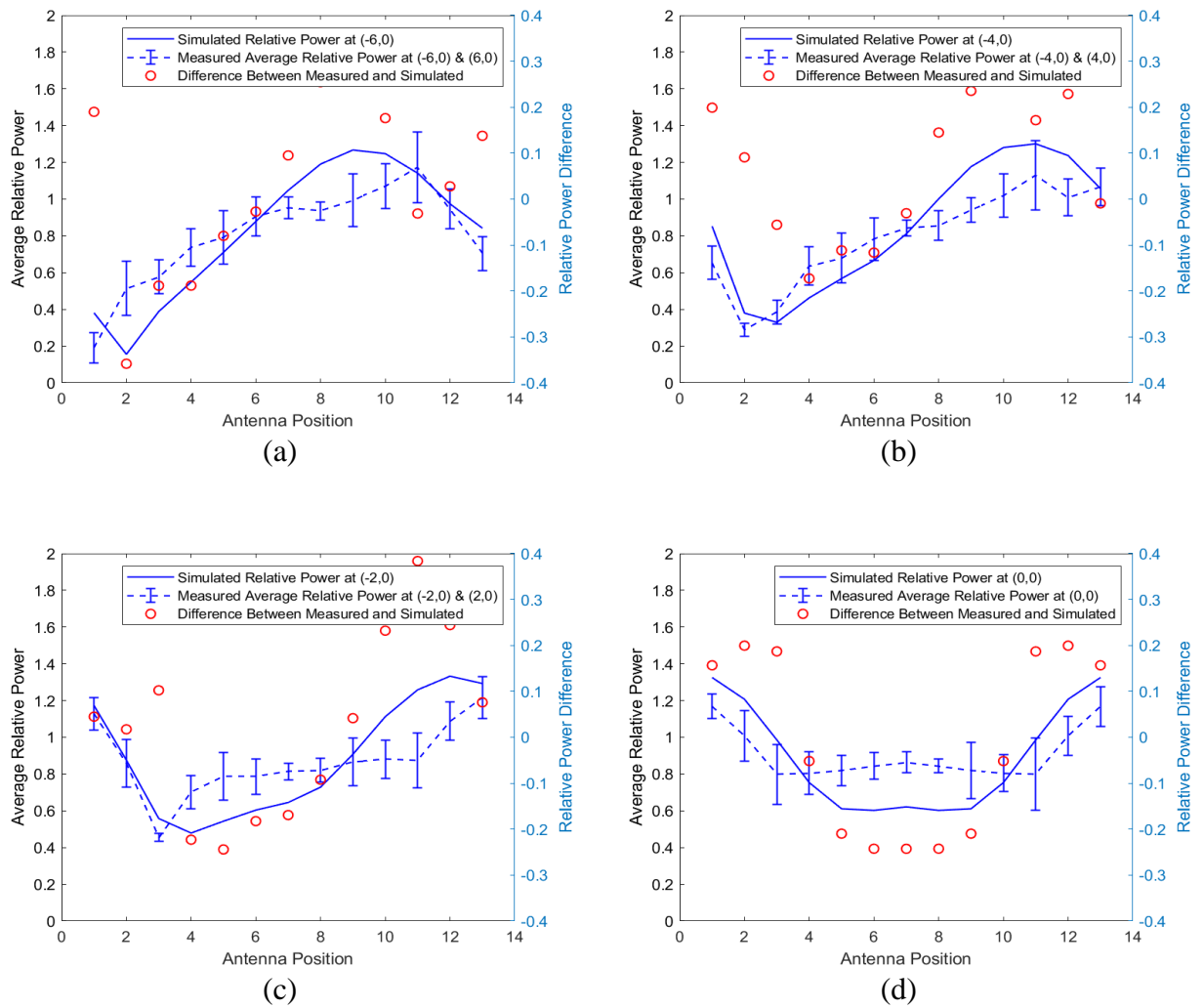
Figure 4.18   (a)-(d) The average relative power (left y-axis) at the receiver array, measured and simulated for the Al rod at symmetrical positions in the scanning plane at 2.5 GHz.

Figure 4.19 shows contour plots of the average relative power for receiver antennas 1 to 7, for as a function of the position of the Al rod in the X-Y scanning plane. The maximum value of the average relative power was 1.63, and the minimum value of the average relative power was -0.65 in the receiver antenna array. The minimum ARP was found in antenna 1, while the maximum ARP occurred in antenna 3, with the variation of ARP as a function of rod position decreasing from antenna 1 to 7. The maximum ARP for antenna number 1 occurred in the diagonal position of the Al rod in the scanning plane. The maximum value shifted to the right for antenna number 2 and so on. For the antenna number 7, the ARP had the symmetrical values for both the left and right of the Y axis when X = 0 of the scanning plane.
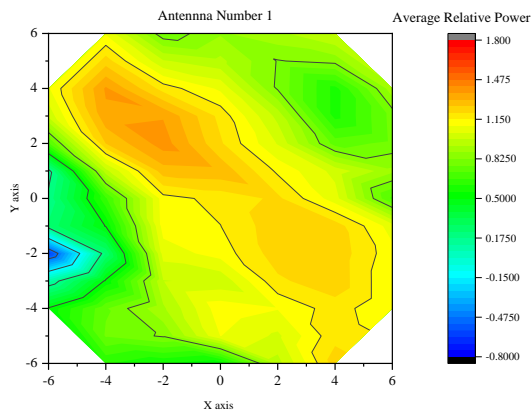
(a)
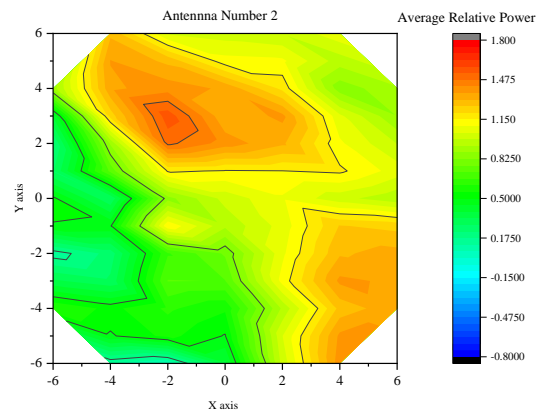
(b)
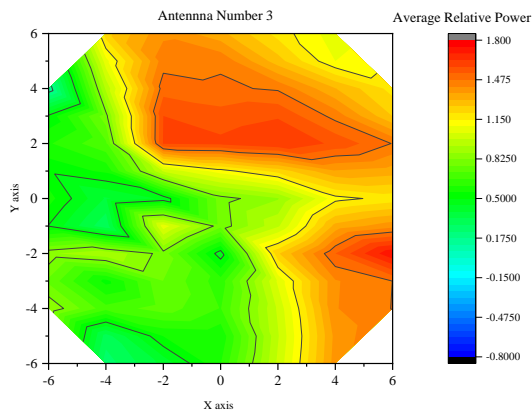
(c)
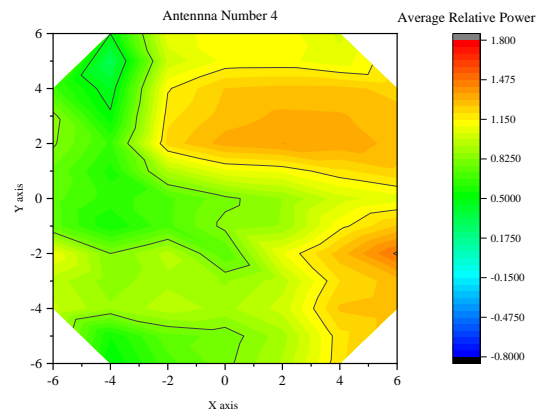
(d)
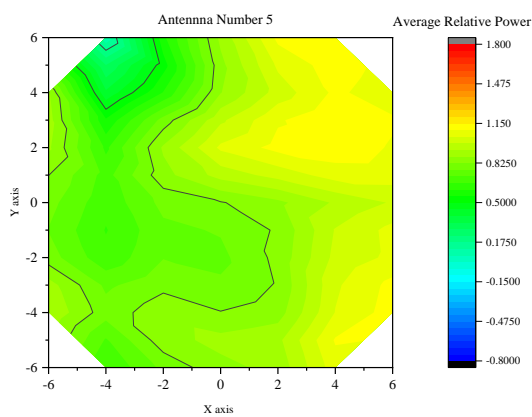
(e)
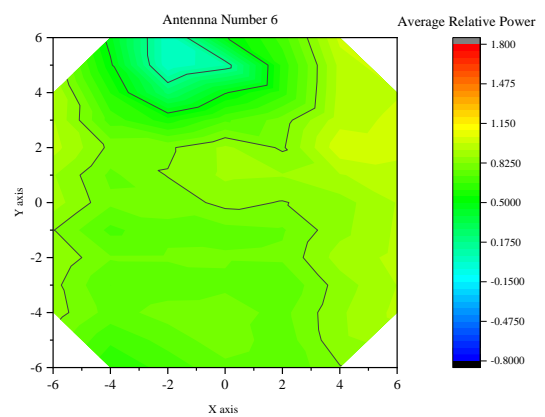
(f)
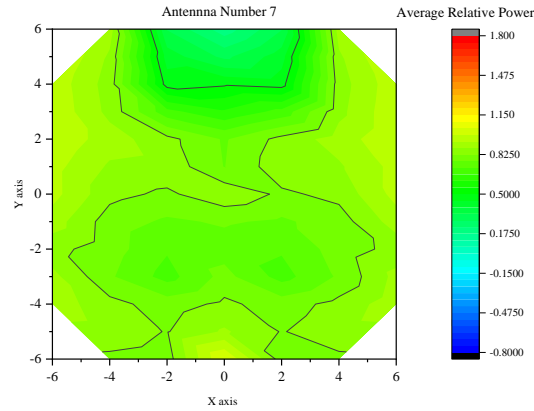
(g)

Figure 4.19   The contour plots of the average relative power (ARP) at receiver antennas 1 to 7, for the Al rod at different positions in the scanning plane at 2.5 GHz frequency.

4.11 Model Validation

The ability to predict the position of the Al rod in the scanning plane using the developed mathematical model had been analyzed by comparing the average relative power (ARP) from the experimental results with the results of the mathematical model. The details of the derived mathematical model, as shown in equation (4.5), can be found in Section 3.3.14 of this thesis. The output of the mathematical model of the portable system, which has three-parameters, C_1, C_2, and C_3, depends on the position of the Al rod in the scanning grid (u and w). These parameters were calculated from the different positions of the Al rod and the angle of the receiver antenna position with respect to the centre of the scanning plane. Figure 4.20 shows the result of both the experimental ARP (blue scatter dots) and the calculated ARP from the derived model (solid red line). The R^2 agreement between the calculated ARP from the derived model and the experimental technique for the different positions in the scanning plane was better than 80%. The Al rod was placed at 83 scanning locations in the scanning plane, with 35 points on the negative X-axis plane, 35 points on the positive X-axis plane and 13 points on the Y-axis. The ARP was symmetrical in the Y-axis of the scanning plane. Hence, the three model parameters (C_1, C_2, and C_3) had 48 positional values for the Al rod position in the scanning plane.
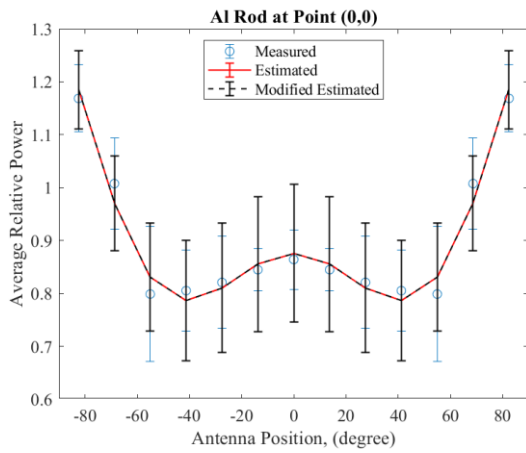
(a)
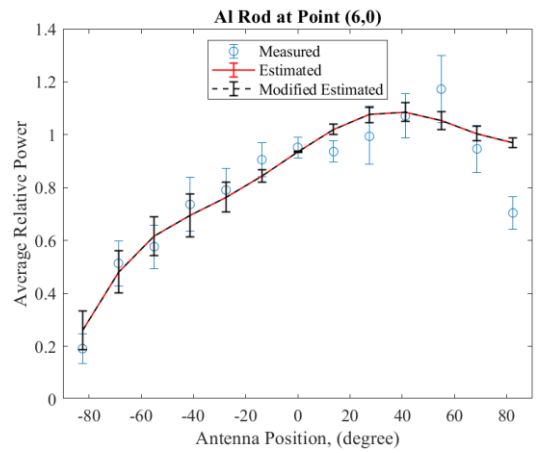
(b)
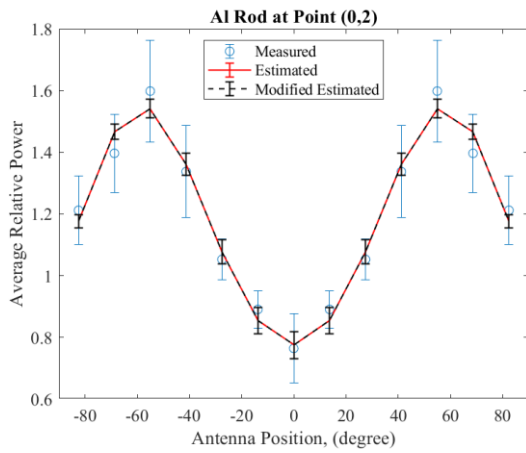
(c)
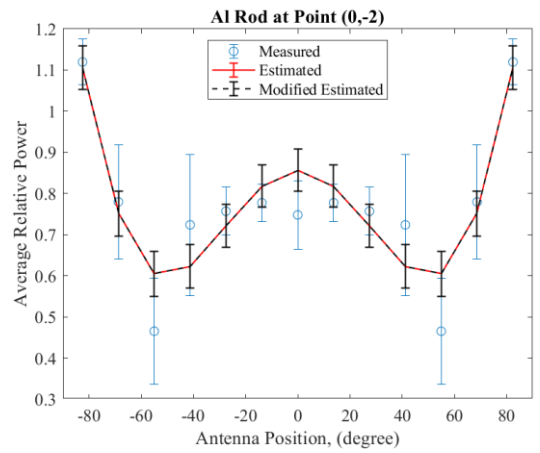
(d)
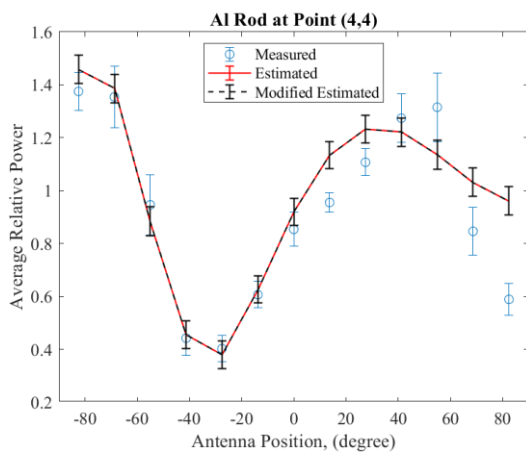
(e)
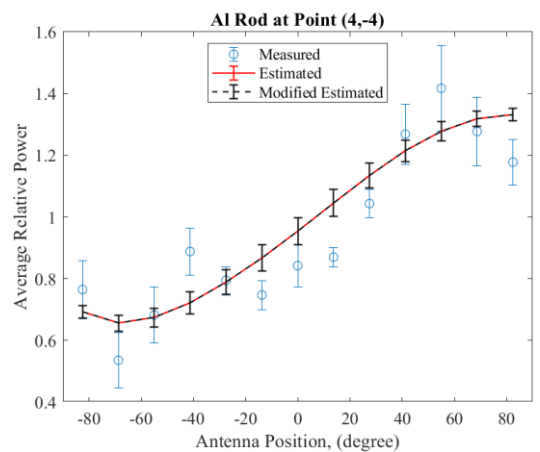
(f)
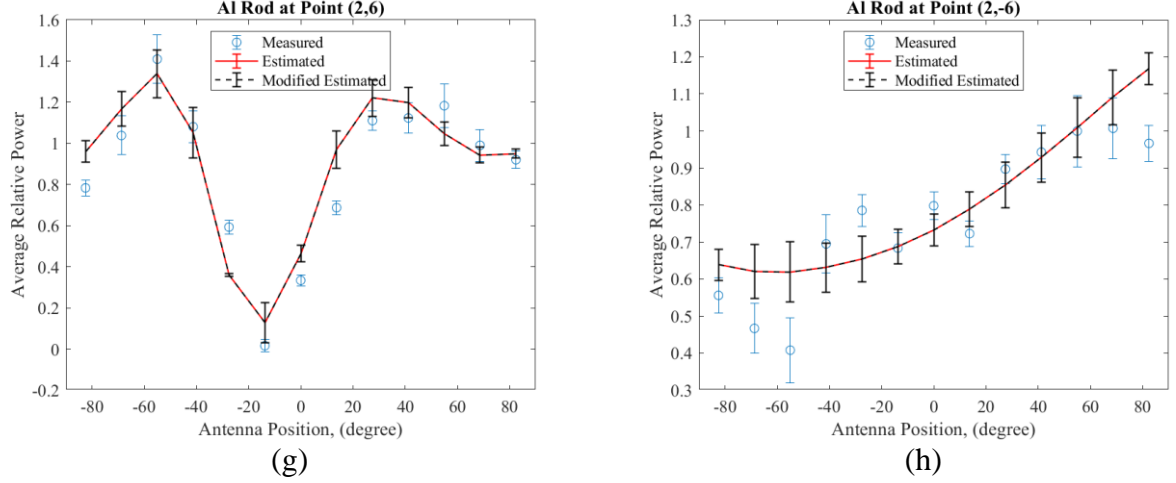
Figure 4.20   (a)-(h) The average relative power (ARP) in the receiver antenna array is shown for the different positions of Al rod in the scanning plane. The dotted lines in these figures indicate the measured ARP for the Al rod. The solid red and dashed black lines represent the estimated and modified estimated ARP from the derived model, and modified model, respectively for the different positions of Al rod.

The average relative power was varied from -0.65 to 1.63. Ratio R from equation 4.5 will be less than one when either the C_1 parameter is negative or cosine term is positive and vise versa. The Curve Fitting Toolbox from MATLAB version 2018a was used to fit the equation (4.5).

$$R = 1 + \left(\frac{C_1}{u\Lambda}\right) \cos\left(C_2(v - w) + C_3\right) + \frac{C_1{}^2}{4u^2\Lambda^2} \tag{4.6}$$

$$\Rightarrow R = 1 + \left(\frac{C_1}{u\Lambda}\right) \cos\left(C_2(v - w)\right) + \frac{C_4{}^2}{4u^2\Lambda^2} \tag{4.7}$$

The C_1 parameters had positive values for the Al rod positions in the scanning plane. For this reason, the phase difference (C_3) was assumed to be zero, and C_1 in the last term of equation (4.5) was replaced by a new parameters C_4, which had the same unit as C_1. Equation (4.6) is the modified version of the derived model of the portable system. The solid black line in Figure 4.20 represents that the ARP for different positions of the Al rod in the scanning plane was calculated based on the modified version of the derived model. The R^2 was better than 85%, illustrating an improved agreement between the calculated ARP from the modified derived model and the experimental technique for the different positions in the scanning plane. The new fitting parameters had 48 points for the different positions of the Al rod. The fitting

parameters and their uncertainties for both general and modified versions of the derived model are given in Appendix ED.
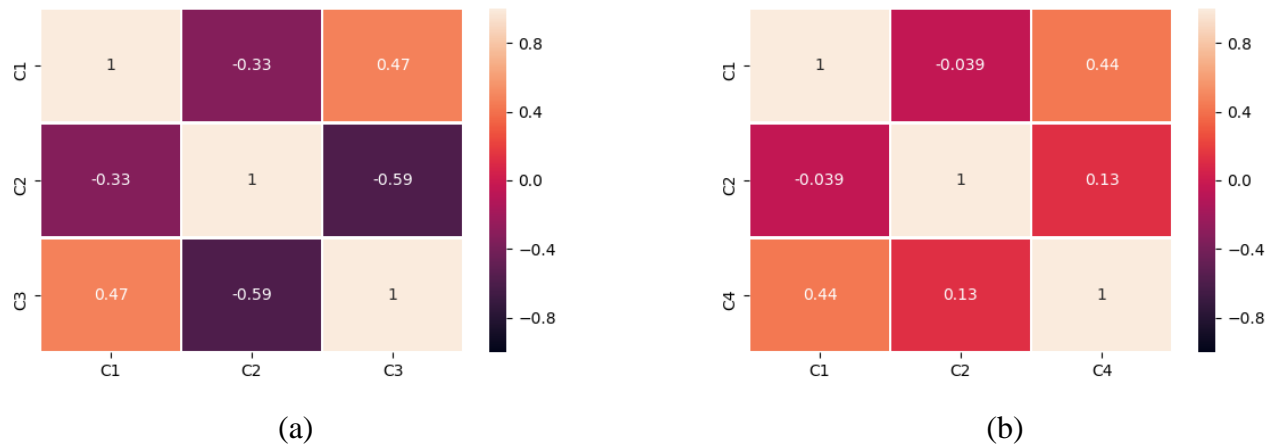
Figure 4.21   The correlation coefficient between each parameter represented by the correlation matrix. (a) general derived model (b) modified derived model for the portable system.

A table of correlation coefficients between each parameter is shown in Figure 4.21. The correlation between two parameters is represented each cell in the correlations table. Figure 4.21 (a) represents the matrix table for the general derived model, showing that for the general derived model C_1 and C_2 had a negative correlation of -0.33. C_2 and C_3 for the general model had a negative relation with each other with a value of -0.59. C_1 and C_2 parameters did not correlate with the modified model shown in Figure 4.21 (b). C_1 and C_4 parameters were positively correlated with each other in the modified model.

CHAPTER V
CONCLUSIONS AND FUTURE WORK

5.1   Summary of Work

In chapter 1, the statistics of breast cancer for the incidence and mortality figures were presented and the various breast cancer screening modalities were described. The established breast screening modalities such as X-mammography, Ultrasound (US), Magnetic Resonance Imaging (MRI) had benefits and drawbacks. As a response to shortcomings, microwave imaging is emerging as a modality due to its low cost, non-ionizing radiation characteristics and high sensitivity.

Breast microwave imaging (MWI) as a novel modality for breast cancer screening is discussed in Chapter 2 where the current state of the different breast MWI systems and their hardware, data acquisition and image reconstruction algorithms are described. For the last two decades, the develop of Breast MWI has focussed on developing systems that can be used in a clinical or hospital. In this thesis, the author has focussed on designing and testing an antenna array that could be incorporated into the development of a new portable breast microwave sensing (BMS) system that could be used in remote locations where no clinical facilities are available for breast cancer screening.

Chapter 3 presented the methods used to develop and evaluate a portable BMS system that could implement a previously simulated portable BMS design by lab members from the non-ionizing research group at the University of Manitoba. Chapter 3 also described the process of selecting the required electrical apparatus for the system to build the main BMS system. The portable BMS system was calibrated using the results from CST studio simulation results. The mathematical model, which was derived using electric field intensity for a point-like scatterer (Al rod) in different scanning chamber positions, was presented.

Chapter 4 showed the results for each step in the process of develop the antenna array for the portable BMS system. The experimental and the calculated results from the derived mathematical model of the system, were compared.

This chapter provides some concluding ideas related to this research as well as recommendations for future work.

5.2   Conclusions

This thesis presented results of a portable breast cancer detection system's response to a point-like scatterer as a function of the frequency of the transmitted microwave signal and the position of the sensors in the receiver array. For the development of the portable BMS system, the distance between the transmitter and the reference antenna receiver antenna was selected 20.00 ± 0.50 cm. The left and the right-side antenna were symmetrical with respect to the reference antenna. From the symmetrical analysis, the estimated differences for 0 cm and 1 cm separated antennas in the receiver were $(0.22 \pm 1.63)\%$ and $(-0.17 \pm 1.74)\%$ at the 95% confidence interval. A semi-circular antenna array using thirteen UWB dual-band PCB antennas with a 4 mm gap between the sensors was developed using the recommendations that the ECC should be less than 0.50. The optimal 4 mm gap resulted in an ECC of 0.37. The one-way ANOVA analysis proved that the 13 sensors in the receiver provided a constant output response with respect to time. While the inherent gain of each symmetrically positioned antenna was approximately equal, the bias factors at 0 dBm input power were different. To overcome this the portable system was calibrated using a $13{\times}10$ array of geometric correction constants, which were estimated from the simulated E-field. The simulated E-fields were, as expected, found to be symmetrical both for the open field and for changes in the position of the Al rod. The measured DC voltages from the sensor as a function of the antenna positions were not well correlated with the simulated E-field because of the different channel bias factor of the RF detectors. For open space comparison, the calculated and measured voltage were approximately the same, with a 96% agreement between the simulated and experimental results. For a point-like scatterer, the calculated and measured voltage had differences of between $\pm$ 15%. The measured power receiver sensor array was ranged from 10.287 dBm to 9.251 dBm for 95% of the expected population, and the horn antenna fed 10 ± 0.35 dBm of power from the signal generator. The average relative power (ARP) difference for the calculated and measured results was varied -0.40 to 0.35. The maximum ARP occurred in the

scanning grid's diagonal position for the number 1 receiver antenna and shifted right for the number 2 antenna and so on. The ARP had equal values for both the left and right sides on the Y-axis of the scanning plane for the antenna 7. The derived mathematical model of the portable BMS system had 80% and 85% agreement with the experimental setup with considering the phase angle and without the phase angle, respectively.

5.3   Suggestions for future work

Improving the agreement between the simulated and experimental measurements will require a more accurate simulation of the experimental conditions. The precise frequency and gain dependent calibration of the antenna/sensor array should provide results as accurate as the simulated results. Once an agreement between sensor and E-field simulations have been obtained, simulated and experimental results will be used to develop a machine learning approach to predict the position of the point-like scatterer in the scanning plane. This research used a homogeneous point-like scatterer instead of the heterogeneous structure of the breast. Ultimately, the portable BMS system's diagnostic performance will have to be evaluated by scanning a morphologically and dielectrically accurate breast phantom.

REFERENCES

[1]   J. Ferlay *et al.*, "Estimating the global cancer incidence and mortality in 2018: GLOBOCAN sources and methods," *Int. J. Cancer*, vol. 144, no. 8, pp. 1941–1953, 2019.

[2]   Ferlay J, Ervik M, Lam F, Colombet M, Mery L, Piñeros M, Znaor A, Soerjomataram I, Bray F (2018), "Global Cancer Observatory: Cancer Today. Lyon, France: International Agency for Research on Cancer". Available from: https://gco.iarc.fr/today, accessed [18 Jan 2020]

[3]   L. A. Torre, R. L. Siegel, E. M. Ward, and A. Jemal, "Global Cancer Incidence and Mortality Rates and Trends—An Update," *Cancer Epidemiol. Prev. Biomark.*, vol. 25, no. 1, pp. 16–27, Jan. 2016.

[4]   C. Allemani *et al.*, "Global surveillance of trends in cancer survival 2000–14 (CONCORD-3): analysis of individual records for 37 513 025 patients diagnosed with one of 18 cancers from 322 population-based registries in 71 countries," *The Lancet*, vol. 391, no. 10125, pp. 1023–1075, Mar. 2018.

[5]   Canadian Cancer Society's Advisory Committee on Cancer Statistics [Internet]. Canadian Cancer Statistics 2019. Toronto, ON: Canadian Cancer Society; 2019. Available at: http://www.cancer.ca/Canadian-Cancer-Statistics-2019-EN (accessed 13 Jan. 2020)

[6]   D. van der Waal, A. L. M. Verbeek, G. J. den Heeten, T. M. Ripping, V. C. G. Tjan-Heijnen, and M. J. M. Broeders, "Breast cancer diagnosis and death in the Netherlands: a changing burden," *Eur. J. Public Health*, vol. 25, no. 2, pp. 320–324, Apr. 2015.

[7]   H. Zhang, "Microwave imaging for ultra-wideband antenna based cancer detection," Ph.D. dissertation, The University of Edinburgh, 2014. Accessed: Jan. 18, 2020. [Online]. Available: https://era.ed.ac.uk/bitstream/handle/1842/9958/Zhang2015.

[8]   M. E. Miller, *Cancer.* 1st ed., Momentum Press, New York, 2018.

[9]   S.-Y. Huang *et al.*, "The characterization of breast anatomical metrics using dedicated breast CT," *Med. Phys.*, vol. 38, no. 4, pp. 2180–2191, Apr. 2011.

[10]   S. Pandya and R. G. Moore, "Breast Development and Anatomy," *Clin. Obstet. Gynecol.*, vol. 54, no. 1, pp. 91–95, Mar. 2011.

[11]   G. F. Schwartz, A. S. Patchefsky, S. A. Feig, G. S. Shaber, and A. B. Schwartz, "Clinically Occult Breast Cancer: Multicentricity and Implications for Treatment," *Ann. Surg.*, vol. 191, no. 1, pp. 8–12, Jan. 1980.

[12]   M. R. Al-Hadidi, A. Alarabeyyat, and M. Alhanahnah, "Breast Cancer Detection Using K-Nearest Neighbor Machine Learning Algorithm," in *2016 9th International Conference on Developments in eSystems Engineering (DeSE)*, pp. 35–39, Aug, 2016.

[13]   E. K. J. Pauwels, N. Foray, and M. H. Bourguignon, "Breast Cancer Induced by X-Ray Mammography Screening? A Review Based on Recent Understanding of Low-Dose Radiobiology," *Med. Princ. Pract.*, vol. 25, no. 2, pp. 101–109, Feb. 2016.

[14]   E. C. Fear, P. M. Meaney, and M. A. Stuchly, "Microwaves for breast cancer detection?" *IEEE Potentials*, vol. 22, no. 1, pp. 12–18, Feb. 2003.

[15]   E. C. Fear, S. C. Hagness, P. M. Meaney, M. Okoniewski, and M. A. Stuchly, "Enhancing breast tumor detection with near-field imaging," *IEEE Microw. Mag.*, vol. 3, no. 1, pp. 48–56, Mar. 2002.

[16]   K. Hoyt, H. Umphrey, M. Lockhart, M. Robbin, and A. Forero-Torres, "Ultrasound Imaging of Breast Tumor Perfusion and Neovascular Morphology," *Ultrasound Med. Biol.*, vol. 41, no. 9, pp. 2292–2302, Sep. 2015.

[17]   L. Sim, J. Hendriks, and S. Fook-Chong, "Breast Ultrasound in Women with Familial Risk of Breast Cancer," vol. 33, no. 5, p. 7, 2004.

[18]   H. D. Cheng, J. Shan, W. Ju, Y. Guo, and L. Zhang, "Automated breast cancer detection and classification using ultrasound images: A survey," *Pattern Recognit.*, vol. 43, no. 1, pp. 299–317, Jan. 2010.

[19]   C. K. Kuhl *et al.*, "Mammography, Breast Ultrasound, and Magnetic Resonance Imaging for Surveillance of Women at High Familial Risk for Breast Cancer," *J. Clin. Oncol.*, vol. 23, no. 33, pp. 8469–8476, Nov. 2005.

[20]   R. M. Mann *et al.*, "Breast MRI: EUSOBI recommendations for women's information," *Eur. Radiol.*, vol. 25, no. 12, pp. 3669–3678, Dec. 2015.

[21]   M. Solis Nepote, "Design, development, and evaluation of a clinical system for breast microwave imaging," MSc. thesis, U of M, Manitoba, 2017. Accessed: Feb. 08, 2020. [Online]. Available: https://mspace.lib.umanitoba.ca/xmlui/handle/1993/32800.

[22]   P. T. Huynh, A. M. Jarolimek, and S. Daye, "The false-negative mammogram," *Radio Graph.*, vol. 18, no. 5, pp. 1137–1154, Sep. 1998.

[23]   A. Martellosio *et al.*, "Dielectric Properties Characterization From 0.5 to 50 GHz of Breast Cancer Tissues," *IEEE Trans. Microw. Theory Tech.*, vol. 65, no. 3, pp. 998–1011, Mar. 2017.

[24]   N. K. Nikolova, "Microwave Imaging for Breast Cancer," *IEEE Microw. Mag.*, vol. 12, no. 7, pp. 78–94, Dec. 2011.

[25]   V. Vorst, A. Rosen, and Y. Kotsuka, *RF/Microwave Interaction with Biological Tissues*, Hoboken. NJ: Wiley 2006.

[26]   A. M. Campbell and D. V. Land, "Dielectric properties of female human breast tissue measured in vitro at 3.2 GHz," *Phys. Med. Biol.*, vol. 37, no. 1, pp. 193–210, Jan. 1992.

[27]   Liewei Sha, E. R. Ward, and B. Stroy, "A review of dielectric properties of normal and malignant breast tissue," in *Proceedings IEEE SoutheastCon 2002 (Cat. No.02CH37283)*, pp. 457–462, Apr. 2002.

[28] T. Sugitani *et al.*, "Complex permittivities of breast tumor tissues obtained from cancer surgeries," *Appl. Phys. Lett.*, vol. 104, no. 25, p. 253702, Jun. 2014.

[29] S. V. Sree, E. Y.-K. Ng, R. U. Acharya, and O. Faust, "Breast imaging: A survey," *World J. Clin. Oncol.*, vol. 2, no. 4, pp. 171–178, Apr. 2011.

[30] D. O'Loughlin, B. L. Oliveira, M. Glavin, E. Jones, and M. O'Halloran, "Advantages and Disadvantages of Parameter Search Algorithms for Permittivity Estimation for Microwave Breast Imaging," in *2019 13th European Conference on Antennas and Propagation (EuCAP)*, Mar. 2019, pp. 1–5.

[31] T. M. Grzegorczyk, P. M. Meaney, P. A. Kaufman, R. M. di Florio-Alexander, and K. D. Paulsen, "Fast 3-D Tomographic Microwave Imaging for Breast Cancer Detection," *IEEE Trans. Med. Imaging*, vol. 31, no. 8, pp. 1584–1592, Aug. 2012, doi: 10.1109/TMI.2012.2197218.

[32] T. Reimer, J. Sacristan, and S. Pistorius, "Improving the Diagnostic Capability of Microwave Radar Imaging Systems using Machine Learning," in *2019 13th European Conference on Antennas and Propagation (EuCAP)*, pp. 1–5, Mar. 2019.

[33] D. O'Loughlin, M. O'Halloran, B. M. Moloney, M. Glavin, E. Jones, and M. A. Elahi, "Microwave Breast Imaging: Clinical Advances and Remaining Challenges," *IEEE Trans. Biomed. Eng.*, vol. 65, no. 11, pp. 2580–2590, Nov. 2018.

[34] Z. Wang, E. G. Lim, Y. Tang, and M. Leach, "Medical Applications of Microwave Imaging," *Sci. World J.*, vol. 2014, pp. 1–7, 2014.

[35] P. M. Meaney *et al.*, "Microwave imaging for neoadjuvant chemotherapy monitoring: initial clinical experience," *Breast Cancer Res.*, vol. 15, no. 2, Apr. 2013.

[36] M. Ostadrahimi *et al.*, "On the development of a clinical full-vectorial 3D microwave breast imaging system," in *2015 USNC-URSI Radio Science Meeting (Joint with AP-S Symposium)*, pp. 300–300, Jul. 2015.

[37] J. C. Lin, "Frequency optimization for microwave imaging of biological tissues," *Proc. IEEE*, vol. 73, no. 2, pp. 374–375, Feb. 1985.

[38] A. Baran, D. J. Kurrant, A. Zakaria, E. C. Fear, and J. LoVetri, "Breast Imaging Using Microwave Tomography with Radar-Based Tissue-Regions Estimation," *Prog. Electromagn. Res.*, vol. 149, pp. 161–171, 2014.

[39] P. M. Meaney, M. W. Fanning, Dun Li, S. P. Poplack, and K. D. Paulsen, "A clinical prototype for active microwave imaging of the breast," *IEEE Trans. Microw. Theory Tech.*, vol. 48, no. 11, pp. 1841–1853, Nov. 2000.

[40] N. R. Epstein, P. M. Meaney, and K. D. Paulsen, "3D parallel-detection microwave tomography for clinical breast imaging," *Rev. Sci. Instrum.*, vol. 85, no. 12, p. 124704, Dec. 2014.

[41] Q. Fang, P. M. Meaney, and K. D. Paulsen, "Viable Three-Dimensional Medical Microwave Tomography: Theory and Numerical Experiments," *IEEE Trans. Antennas Propag.*, vol. 58, no. 2, pp. 449–458, Feb. 2010.

[42] E. C. Fear, J. Bourqui, C. Curtis, D. Mew, B. Docktor, and C. Romano, "Microwave Breast Imaging with a Monostatic Radar-Based System: A Study of Application to Patients," *IEEE Trans. Microw. Theory Tech.*, vol. 61, no. 5, pp. 2119–2128, May 2013.

[43] J. Bourqui, M. Okoniewski, and E. C. Fear, "Balanced Antipodal Vivaldi Antenna with Dielectric Director for Near-Field Microwave Imaging," *IEEE Trans. Antennas Propag.*, vol. 58, no. 7, pp. 2318–2326, Jul. 2010.

[44] J. Bourqui, J. M. Sill, and E. C. Fear, "A Prototype System for Measuring Microwave Frequency Reflections from the Breast," *Int. J. Biomed. Imaging*, vol. 2012, pp. 1–12, 2012.

[45] A. W. Preece, I. Craddock, M. Shere, L. Jones, and H. L. Winton, "MARIA M4: clinical evaluation of a prototype ultrawideband radar scanner for breast cancer detection," *J. Med. Imaging*, vol. 3, no. 3, p. 033502, Jul. 2016.

[46] M. Klemm *et al.*, "Development and testing of a 60-element UWB conformal array for breast cancer imaging," in *Proceedings of the 5th European Conference on Antennas and Propagation (EUCAP)*, pp. 3077–3079, Apr. 2011.

[47] E. Porter, A. Santorelli, M. Coates, and M. Popović, "Time-Domain Microwave Breast Cancer Detection: Extensive System Testing with Phantoms," *Technol. Cancer Res. Treat.*, vol. 12, no. 2, pp. 131–143, Apr. 2013.

[48] E. Porter, E. Kirshin, A. Santorelli, M. Coates, and M. Popović, "Time-Domain Multistatic Radar System for Microwave Breast Screening," *IEEE Antennas Wirel. Propag. Lett.*, vol. 12, pp. 229–232, 2013.

[49] T. Reimer, M. Solis-Nepote, and S. Pistorius, "The Application of an Iterative Structure to the Delay-and-Sum and the Delay-Multiply-and-Sum Beamformers in Breast Microwave Imaging," *Diagnostics*, vol. 10, no. 6, p. 411, Jun. 2020.

[50] S. C. Hagness, A. Taflove, and J. E. Bridges, "Three-dimensional FDTD analysis of a pulsed microwave confocal system for breast cancer detection: design of an antenna-array element," *IEEE Trans. Antennas Propag.*, vol. 47, no. 5, pp. 783–791, May 1999.

[51] R. Nilavalan, I. J. Craddock, A. Preece, J. Leendertz, and R. Benjamin, "Wideband microstrip patch antenna design for breast cancer tumour detection," *Antennas Propag. IET Microw.*, vol. 1, no. 2, pp. 277–281, Apr. 2007.

[52] T. Rubaek, O. S. Kim, and P. Meincke, "Computational Validation of a 3-D Microwave Imaging System for Breast-Cancer Screening," *IEEE Trans. Antennas Propag.*, vol. 57, no. 7, pp. 2105–2115, Jul. 2009.

[53] B. J. Mohammed, A. M. Abbosh, and P. Sharpe, "Planar array of corrugated tapered slot antennas for ultrawideband biomedical microwave imaging system," *Int. J. RF Microw. Comput. Aided Eng.*, vol. 23, no. 1, pp. 59–66, 2013.

[54] M. T. Islam, Md. Z. Mahmud, N. Misran, J.-I. Takada, and M. Cho, "Microwave Breast Phantom Measurement System with Compact Side Slotted Directional Antenna," *IEEE Access*, vol. 5, pp. 5321–5330, 2017.

[55] J. Sacristan, "Preliminary study of a mobile microwave breast cancer detection device using machine learning," MSc. Thesis, U of M, Manitoba, 2017. Accessed: Apr. 06, 2020. [Online]. Available: https://mspace.lib.umanitoba.ca/xmlui/handle/1993/32777

[56] L. Fu et al., "Microwave radar imaging using a solid state spintronic microwave sensor," *Appl. Phys. Lett.*, vol. 105, no. 12, p. 122406, Sep. 2014.

[57] Z. X. Cao, W. Lu, L. Fu, Y. S. Gui, and C.-M. Hu, "Spintronic microwave imaging," *Appl. Phys. A*, vol. 111, no. 2, pp. 329–337, May 2013.

[58] N. A. Hassan, M. M. Mohamed, and M. B. Tayel, "Basic Evaluation of Antennas Used in Microwave Imaging for Breast Cancer Detection," in *Computer Science & Information Technology (CS & IT)*, pp. 55–63, Aug. 2016.

[59] J. Liu, Z. Tang, Z. Wang, H. Li, and Y. Yin, "Gain Enhancement of a Broadband Symmetrical Dual-Loop Antenna Using Shorting Pins," IEEE Antennas Wirel. Propag. Lett., vol. 17, no. 8, pp. 1369–1372, Aug. 2018.

[60] Molex Electronics Solutions, "Ultra-Wideband (UWB) PCB Antenna with Balanced Transmission," 146184 UWB datasheet, 2016. Accessed on: Jun. 03, 2020. [Online] Available: https://www.ttiinc.com/content/dam/ttiinc/manufacturers/molex/pdf/molex-UWB antenna.pdf

[61] Analog Devices, "Dual Log Detector/Controller," ADL5519 datasheet, 2008. [Revised 2020] Accessed on: Jun. 03, 2020. [Online] Available: https://www.analog.com/media/en/technical-documentation/data-sheets/ADL5519.pdf

[62] Vaunix Technology Corporation, "Lab Brick RF and Microwave USB Programmable Signal Generators," LSG-602 datasheet, Dec 2009. Accessed on: Jun. 04, 2020. [Online] Available: https://vaunix.com/resources/lsg%20signal%20generators-datasheet.pdf

[63] D. R. Herrera, "Antenna Characterisation and Optimal Sampling Constraints for Breast Microwave Imaging Systems with a Novel Wave Speed Propagation Algorithm," MSc., U of M, Manitoba, 2016. Accessed: Apr. 06, 2020 [Online]. Available: https://mspace.lib.umanitoba.ca/xmlui/handle/1993/31907

[64] J. J. Carr, *Microwave and Wireless Communications Technology*. 1st ed., Woburn, MA: Newnes 1997.

[65] A. Pewsey, "Testing circular symmetry," *Can. J. Stat.*, vol. 30, no. 4, pp. 591–600, 2002.

[66] M. Wang, W. Wu, and Z. Shen, "Bandwidth Enhancement of Antenna Arrays Utilizing Mutual Coupling between Antenna Elements," *Int. J. Antennas Propag.*, vol. 2010, Jan. 2010.

[67] C.-X. Mao and Q.-X. Chu, "Compact Coradiator UWB-MIMO Antenna with Dual Polarization," *IEEE Trans. Antennas Propag.*, vol. 62, no. 9, pp. 4474–4480, Sep. 2014.

[68] R. G. Vaughan and J. B. Andersen, "Antenna diversity in mobile communications," *IEEE Trans. Veh. Technol.*, vol. 36, no. 4, pp. 149–172, Nov. 1987.

[69] G. Srivastava and A. Mohan, "Compact MIMO Slot Antenna for UWB Applications," *IEEE Antennas Wirel. Propag. Lett.*, vol. 15, pp. 1057–1060, 2016.

[70] Constantine A. Balanis, *Antenna Theory: Analysis and Design*. 4th ed., John Wiley & Sons, Inc, 2016.

[71] R. Jedlicka, M. Poe, and K. Carver, "Measured mutual coupling between microstrip antennas," *IEEE Trans. Antennas Propag.*, vol. 29, no. 1, pp. 147–149, Jan. 1981.

APPENDIX A

VAUNIX LAB BRICK SIGNAL GENERATOR LICENSE CODE

The following Python code used to control the lab signal generators for different frequency points with a certain period.

```
vnx = cdll.vnx_fsynth   ##access the DLL
vnx.fnLSG_SetTestMode(0) ## turn off the DLL's simulation test mode
DeviceIDArray = c_int * 64  ## the array just must be big enough for the number of devices you expect – 20 is fine, 64 is probably more than you need
Devices = DeviceIDArray ()
print ("Number of devices =", vnx.fnLSG_GetNumDevices())  ## tell the DLL to go out and find the hardware, it returns the number of devices found
vnx.fnLSG_GetDevInfo(Devices) ## get a list of active device handles from the DLL – one for each connected device
print ("Serial Number", vnx.fnLSG_GetSerialNumber(Devices[0])) ## print the serial number of the first connected device
vnx.fnLSG_InitDevice(Devices[0])  ## get any LSG device you want to use
vnx.fnLSG_SetRFOn(Devices[0], False) ## turn off the signal generator
freq_var = 14000 ## initial frequency and 14000 equals to 1.4 GHz
samplefreq = 1
vnx.fnLSG_SetRFOn(Devices[0], True) ## turn on the signal generator
print(vnx.fnLSG_GetDeviceStatus(Devices[0])) ## print the status signal generator
for i in range (47):
    vnx.fnLSG_SetFrequency(Devices[0], freq_var) ## controlling the frequency setup for the signal generator
    print ("Frequency in GHz =", (vnx.fnLSG_GetFrequency(Devices[0]))) ## print the frequency point
    vnx.fnLSG_SetPowerLevel(Devices[0], 40) ## initial power and 40 equal to 10 dBm
    print ("Output Power in dBm =", vnx.fnLSG_GetPowerLevel(Devices[0])) ## print the power level
    print(vnx.fnLSG_GetDeviceStatus(Devices[0]))
    freq_var += 1000    ## 0.1 GHz frquency increment
```

```
    time.sleep(1/samplefreq) ## time sampling of 1 second
    print(i)
vnx.fnLSG_SetFrequency(Devices[0], 15000)
print ("Frequency in GHz =", (vnx.fnLSG_GetFrequency(Devices[0])))
vnx.fnLSG_SetRFOn(Devices[0], False) ## turn off the signal generator
vnx.fnLSG_CloseDevice(Devices[0])  ## disconnect the signal generator from the computer
```

APPENDIX B

LINEAR PARAMETERS

Linear Parameters such as gain (A) and bias factor (B) are presented in Table B.1 and Table B.2 respectively for 13 receiver sensors from 1.5 GHz to 6 GHz with an interval of 0.5 GHz.

Table B.1   Gain, A (-1×10^{-2}) (dBm/Volts) for 13 sensors and 10 frequency points with two standard deviations.

		Frequency (GHz)									
		1.5	2	2.5	3	3.5	4	4.5	5	5.5	6
Antenna Position	1	2.25 ± 0.14	2.22 ± 0.14	2.26 ± 0.02	2.21 ± 0.04	2.30 ± 0.34	2.29 ± 0.14	2.32 ± 0.06	2.34 ± 0.34	2.40 ± 0.08	2.37 ± 0.10
	2	2.11 ± 0.12	2.14 ± 0.38	2.19 ± 0.12	2.15 ± 0.06	2.22 ± 0.06	2.21 ± 0.28	2.22 ± 0.12	2.20 ± 0.02	2.33 ± 0.16	2.14 ± 0.22
	3	2.12 ± 0.42	2.09 ± 0.16	2.19 ± 0.12	2.16 ± 0.08	2.19 ± 0.14	2.16 ± 0.16	2.20 ± 0.06	2.22 ± 0.14	2.26 ± 0.06	2.21 ± 0.18
	4	2.24 ± 0.28	2.15 ± 0.78	2.19 ± 0.10	2.19 ± 0.12	2.17 ± 0.24	2.22 ± 0.06	2.16 ± 0.10	2.14 ± 0.24	2.07 ± 0.26	2.16 ± 0.22
	5	2.17 ± 0.16	2.12 ± 0.06	2.13 ± 0.06	2.13 ± 0.08	2.17 ± 0.06	2.16 ± 0.16	2.16 ± 0.08	2.15 ± 0.04	2.19 ± 0.14	2.17 ± 0.10
	6	2.09 ± 0.42	2.14 ± 0.16	2.14 ± 0.06	2.15 ± 0.02	2.18 ± 0.18	2.15 ± 0.04	2.17 ± 0.10	2.16 ± 0.04	2.21 ± 0.02	2.21 ± 0.06
	7	2.21 ± 0.10	2.18 ± 0.28	2.19 ± 0.06	2.19 ± 0.02	2.24 ± 0.1	2.22 ± 0.02	2.23 ± 0.06	2.26 ± 0.02	2.31 ± 0.18	2.27 ± 0.10
	8	2.17 ± 0.18	2.14 ± 0.36	2.16 ± 0.02	2.16 ± 0.04	2.22 ± 0.04	2.18 ± 0.06	2.19 ± 0.02	2.21 ± 0.02	2.24 ± 0.12	2.24 ± 0.04
	9	2.11 ± 0.22	2.12 ± 0.04	2.13 ± 0.02	2.12 ± 0.04	2.15 ± 0.28	2.14 ± 0.32	2.14 ± 0.02	2.15 ± 0.02	2.18 ± 0.04	2.17 ± 0.14
	10	2.19 ± 0.22	2.18 ± 0.38	2.17 ± 0.12	2.16 ± 0.08	2.18 ± 0.2	2.18 ± 0.18	2.16 ± 0.1	2.15 ± 0.14	2.12 ± 0.34	2.11 ± 0.36
	11	2.14 ± 0.18	2.10 ± 0.24	2.14 ± 0.3	2.11 ± 0.12	2.11 ± 0.06	2.13 ± 0.06	2.13 ± 0.04	2.19 ± 0.12	2.21 ± 0.06	2.21 ± 0.04
	12	2.22 ± 0.16	2.21 ± 0.24	2.22 ± 0.10	2.21 ± 0.08	2.24 ± 0.16	2.22 ± 0.30	2.25 ± 0.04	2.28 ± 0.08	2.28 ± 0.28	2.18 ± 0.16
	13	2.15 ± 0.46	2.16 ± 0.24	2.19 ± 0.06	2.17 ± 0.08	2.22 ± 0.32	2.26 ± 0.26	2.25 ± 0.04	2.27 ± 0.42	2.32 ± 0.06	2.33 ± 0.10

Table B.2   Bias factor, *B* (Volts) for 13 sensors and 10 frequency points with two standard deviations.

		Frequency (GHz)									
		1.5	2	2.5	3	3.5	4	4.5	5	5.5	6
Antenna Position	1	1.075 ± 0.018	0.995 ± 0.018	0.956 ± 0.004	0.928 ± 0.004	0.991 ± 0.038	0.999 ± 0.014	0.895 ± 0.008	0.979 ± 0.044	0.999 ± 0.008	1.052 ± 0.014
	2	1.182 ± 0.016	1.137 ± 0.048	1.021 ± 0.014	0.931 ± 0.006	0.896 ± 0.008	0.961 ± 0.032	0.901 ± 0.012	0.822 ± 0.002	1.038 ± 0.022	1.185 ± 0.038
	3	1.157 ± 0.054	0.965 ± 0.018	0.979 ± 0.016	0.917 ± 0.008	0.882 ± 0.018	0.813 ± 0.018	0.939 ± 0.006	0.902 ± 0.016	0.977 ± 0.006	1.026 ± 0.022
	4	1.163 ± 0.036	1.171 ± 0.098	0.952 ± 0.01	0.995 ± 0.018	0.945 ± 0.026	0.827 ± 0.011	0.806 ± 0.008	0.921 ± 0.024	1.056 ± 0.022	1.028 ± 0.016
	5	1.073 ± 0.018	0.924 ± 0.008	0.856 ± 0.008	0.876 ± 0.011	0.861 ± 0.006	0.822 ± 0.018	0.806 ± 0.011	0.786 ± 0.006	0.896 ± 0.018	0.991 ± 0.014
	6	1.136 ± 0.052	1.005 ± 0.022	0.825 ± 0.008	0.823 ± 0.002	0.881 ± 0.022	0.786 ± 0.006	0.817 ± 0.011	0.797 ± 0.004	0.888 ± 0.002	0.955 ± 0.008
	7	1.119 ± 0.012	1.058 ± 0.034	0.848 ± 0.006	0.871 ± 0.002	0.934 ± 0.014	0.812 ± 0.004	0.814 ± 0.008	0.886 ± 0.002	0.992 ± 0.022	1.075 ± 0.012
	8	1.026 ± 0.022	1.064 ± 0.048	0.831 ± 0.002	0.835 ± 0.006	0.925 ± 0.004	0.811 ± 0.006	0.814 ± 0.002	0.828 ± 0.002	0.912 ± 0.014	0.956 ± 0.004
	9	1.112 ± 0.026	0.937 ± 0.006	0.834 ± 0.004	0.861 ± 0.004	0.919 ± 0.034	0.831 ± 0.042	0.783 ± 0.002	0.783 ± 0.002	0.894 ± 0.004	1.001 ± 0.018
	10	1.178 ± 0.024	1.064 ± 0.046	0.948 ± 0.012	0.949 ± 0.008	0.929 ± 0.022	0.859 ± 0.011	0.805 ± 0.012	0.937 ± 0.016	1.037 ± 0.036	1.018 ± 0.031
	11	1.089 ± 0.022	1.006 ± 0.03	0.981 ± 0.034	0.906 ± 0.012	0.888 ± 0.004	0.804 ± 0.008	0.897 ± 0.002	0.908 ± 0.016	0.981 ± 0.008	1.005 ± 0.004
	12	1.115 ± 0.022	0.994 ± 0.026	1.024 ± 0.012	0.927 ± 0.011	0.924 ± 0.022	1.008 ± 0.036	0.917 ± 0.006	0.844 ± 0.011	1.086 ± 0.036	1.192 ± 0.028
	13	1.117 ± 0.062	1.007 ± 0.032	0.935± 0.008	0.897 ± 0.008	0.989 ± 0.038	0.929 ± 0.031	0.856 ± 0.004	0.923 ± 0.052	0.987 ± 0.008	1.053 ± 0.012

APPENDIX C

GEOMETRIC CORRELATION CONSTANTS

The geometric correlation constants, *C* is given in Table C.1 for the 13 receiver antenna positions from 1.5 GHz to 6 GHz with an interval of 0.5 GHz.

Table C.3~~1~~   Geometric correlation constants *C* ($W^{0.5}$m/V) for 13 receiver antenna positions and 10 frequency points from CST Studio Suite 2019 simulation.

		Frequency (GHz)									
		1.5	2	2.5	3	3.5	4	4.5	5	5.5	6
Antenna Position	1	41.30	53.47	56.16	64.16	67.04	69.08	66.56	66.14	51.90	53.50
	2	39.73	51.45	53.70	60.75	64.56	67.49	70.16	66.49	59.41	58.87
	3	37.49	49.67	52.65	60.57	65.02	64.61	73.06	71.11	70.99	65.46
	4	35.62	49.18	51.00	59.49	66.91	64.50	76.37	72.57	77.70	73.70
	5	34.47	50.09	50.82	58.26	65.79	61.71	78.42	77.88	89.68	85.37
	6	34.11	51.10	51.94	58.07	64.39	60.47	79.79	79.29	95.35	93.26
	7	34.00	51.41	52.42	57.79	63.32	60.28	80.52	78.59	94.80	92.68
	8	34.11	51.10	51.94	58.07	64.39	60.47	79.79	79.29	95.35	93.26
	9	34.47	50.09	50.82	58.26	65.79	61.71	78.42	77.88	89.68	85.37
	10	35.62	49.18	51.00	59.49	66.91	64.50	76.37	72.57	77.70	73.70
	11	37.49	49.67	52.65	60.57	65.02	64.61	73.06	71.11	70.99	65.46
	12	39.73	51.45	53.70	60.75	64.56	67.49	70.16	66.49	59.41	58.87
	13	41.30	53.47	56.16	64.16	67.04	69.08	66.56	66.14	51.90	53.50

APPENDIX D

CALIBRATION CONSTANTS

The calibration constants, C is given in Table D.1 for the 13 receiver antenna positions from 1.5 GHz to 6 GHz with an interval of 0.5 GHz.

Table D.~~1~~1   Calibration constants C (V/dBm) for 13 receiver antenna positions and 10 frequency points.

		Frequency (GHz)									
		1.5	2	2.5	3	3.5	4	4.5	5	5.5	6
Antenna Position	1	0.08	0.08	0.08	0.08	0.08	0.08	0.08	0.08	0.08	0.08
	2	0.08	0.08	0.08	0.08	0.08	0.08	0.08	0.08	0.08	0.08
	3	0.07	0.08	0.08	0.07	0.08	0.07	0.07	0.07	0.07	0.08
	4	0.08	0.08	0.08	0.08	0.08	0.08	0.08	0.08	0.08	0.08
	5	0.07	0.07	0.07	0.07	0.07	0.07	0.07	0.07	0.07	0.07
	6	0.07	0.07	0.07	0.07	0.07	0.07	0.07	0.07	0.07	0.07
	7	0.07	0.07	0.07	0.07	0.07	0.07	0.07	0.07	0.07	0.07
	8	0.07	0.07	0.07	0.07	0.07	0.07	0.07	0.07	0.07	0.07
	9	0.07	0.07	0.07	0.07	0.07	0.07	0.07	0.07	0.07	0.08
	10	0.08	0.08	0.08	0.08	0.08	0.08	0.08	0.08	0.08	0.08
	11	0.07	0.08	0.07	0.07	0.07	0.07	0.07	0.07	0.07	0.07
	12	0.08	0.08	0.08	0.08	0.08	0.08	0.08	0.08	0.08	0.08
	13	0.08	0.08	0.08	0.08	0.08	0.07	0.07	0.08	0.07	0.07

APPENDIX E

FITTING PARAMETERS

The fitting parameters and their uncertainties for both general and modified versions of the derived mathematical model of the portable BMS system are presented in Table D.1 and D.2.

Table E.5~~1~~ C_1, C_2, C_3 fitting parameters at 48 scanning positions of the Al rod in the scanning plane for the general mathematical model of the portable BMS system.

Al rod Point (x, y)	$C_1 \times 10^{-3}$	C_2	C_3
(0, 0)	9.09 ± 0.32	16.98 ± 1.52	0.99 ± 0.09
(2, 0)	0.77 ± 0.34	47.83 ± 3.19	-1.96 ± 0.72
(4, 0)	1.12 ± 0.45	31.71 ± 2.93	-0.68 ± 0.37
(6, 0)	0.71 ± 0.35	48.09 ± 4.15	-2.37 ± 0.41
(0, 1)	2.19 ± 1.53	15.03 ± 1.13	0.15 ± 0.53
(2, 1)	1.13 ± 0.51	27.57 ± 1.49	-1.34 ± 0.25
(4, 1)	1.44 ± 0.72	28.44 ± 2.18	-1.19 ± 0.27
(6, 1)	0.78 ± 0.44	41.81 ± 3.13	-1.92 ± 0.57
(0, 2)	1.91 ± 0.16	45.81 ± 3.98	-3.89 ± 0.08
(2, 2)	2.11 ± 0.79	32.46 ± 2.75	-2.33 ± 0.31
(4, 2)	1.82 ± 1.41	28.58 ± 0.44	-1.56 ± 0.41
(6, 2)	0.65 ± 0.59	38.17 ± 3.55	-2.31 ± 0.11
(0, 3)	1.89 ± 0.21	42.31 ± 4.16	-3.67 ± 0.09
(2, 3)	2.48 ± 0.97	32.52 ± 2.96	-2.26 ± 0.11
(4, 3)	1.81 ± 1.11	30.44 ± 1.51	-2.03 ± 0.31
(6, 3)	0.31 ± 0.63	17.91 ± 4.19	0.02 ± 0.01
(0, 4)	-1.98 ± 0.14	39.69 ± 2.41	-6.62 ± 0.05
(2, 4)	1.87 ± 0.76	39.93 ± 0.62	-3.46 ± 0.30
(4, 4)	1.54 ± 0.77	33.56 ± 5.26	-2.71 ± 0.27
(6, 4)	0.34 ± 0.48	32.71 ± 5.52	-2.53 ± 0.95
(0, 5)	1.56 ± 0.49	46.38 ± 5.20	-4.53 ± 0.25
(2, 5)	1.44 ± 0.57	39.97 ± 5.99	-3.83 ± 0.29
(4, 5)	1.03 ± 0.30	38.52 ± 1.22	-3.71 ± 0.18
(0, 6)	1.51 ± 0.53	36.49 ± 5.75	-3.58 ± 0.14
(2, 6)	1.01 ± 0.49	45.47 ± 1.56	-5.01 ± 0.35
(4, 6)	0.78 ± 0.23	42.71 ± 1.21	-4.65 ± 0.19
(0, -1)	8.94 ± 0.88	16.21 ± 3.85	1.21 ± 0.03
(2, -1)	5.51 ± 1.23	11.19 ± 2.91	1.19 ± 0.03
(4, -1)	1.74 ± 0.78	31.71 ± 4.11	-0.81 ± 0.24
(6, -1)	1.52 ± 0.69	27.49 ± 3.94	-0.65 ± 0.29
(0, -2)	9.24 ± 0.25	29.93 ± 0.55	0.65 ± 0.07
(2, -2)	0.67 ± 0.53	60.42 ± 6.14	-2.89 ± 0.76
(4, -2)	-1.61 ± 0.97	67.55 ± 1.95	-5.86 ± 0.28

(6, -2)	1.51 ± 2.94	32.56 ± 1.43	-1.23 ± 0.85
(0, -3)	8.78 ± 0.19	26.71 ± 2.24	-5.15 ± 0.08
(2, -3)	2.35 ± 2.25	13.84 ± 1.56	0.95 ± 0.11
(4, -3)	1.81 ± 1.11	34.53 ± 4.98	-0.63 ± 0.31
(6, -3)	1.98 ± 1.21	28.91 ± 0.96	-0.41 ± 0.29
(0, -4)	7.75 ± 0.34	39.34 ± 1.63	0.68 ± 0.13
(2, -4)	0.43 ± 0.77	41.66 ± 0.31	-0.17 ± 0.95
(4, -4)	1.98 ± 1.71	23.58 ± 4.13	0.31 ± 0.21
(6, -4)	2.16 ± 1.24	24.02 ± 2.51	0.06 ± 0.21
(0, -5)	6.31 ± 0.24	58.91 ± 5.89	-0.02 ± 0.11
(2, -5)	0.98 ± 0.41	24.59 ± 1.71	0.78 ± 0.64
(4, -5)	3.56 ± 1.11	19.85 ± 3.27	1.01 ± 0.04
(0, -6)	4.79 ± 0.27	42.75 ± 5.01	1.52 ± 0.15
(2, -6)	-1.03 ± 0.56	30.53 ± 2.46	-2.43 ± 0.41
(4, -6)	2.35 ± 0.26	27.89 ± 4.13	0.81 ± 0.18

Table E.62 C_1, C_2, C_4 fitting parameters at 48 scanning position of the Al rod in the scanning plane for the modified mathematical model of the portable BMS system.

Al rod Point (x, y)	$C_1 \times 10^{-3}$	C_2	$C_4 \times 10^{-3}$
(0, 0)	3.11 ± 0.55	30.02 ± 0.09	8.73 ± 0.36
(2, 0)	1.48 ± 1.57	25.54 ± 1.50	4.13 ± 7.53
(4, 0)	0.91 ± 0.55	18.60 ± 1.05	2.88 ± 5.15
(6, 0)	0.62 ± 0.21	25.60 ± 2.28	0.62 ± 0.21
(0, 1)	-0.84 ± 0.25	44.27 ± 0.31	0.84 ± 0.25
(2, 1)	1.97 ± 0.43	17.17 ± 0.55	2.86 ± 3.28
(4, 1)	2.13 ± 0.73	15.55 ± 0.57	0.28 ± 2.61
(6, 1)	1.16 ± 1.31	13.98 ± 0.74	0.74 ± 1.67
(0, 2)	-1.95 ± 0.23	39.59 ± 0.12	1.95 ± 0.23
(2, 2)	4.03 ± 1.97	14.60 ± 1.19	2.63 ± 7.15
(4, 2)	2.82 ± 1.75	13.17 ± 0.88	0.05 ± 4.06
(6, 2)	1.25 ± 1.71	11.71 ± 0.66	0.64 ± 1.83
(0, 3)	-1.96 ± 0.22	38.33 ± 0.08	1.96 ± 0.22
(2, 3)	5.23 ± 2.21	14.25 ± 0.61	2.36 ± 3.51
(4, 3)	3.03 ± 1.87	13.38 ± 0.63	0.85 ± 2.63
(6, 3)	0.48 ± 1.06	10.72 ± 1.01	1.04 ± 3.29
(0, 4)	3.41 ± 1.42	08.84 ± 1.04	2.98 ± 6.21
(2, 4)	3.84 ± 2.76	12.11 ± 0.88	0.47 ± 4.86
(4, 4)	2.85 ± 1.81	12.44 ± 0.43	0.61 ± 1.54
(6, 4)	0.82 ± 0.72	11.40 ± 0.25	0.04 ± 0.38
(0, 5)	2.86 ± 1.26	11.33 ± 0.81	0.33 ± 4.49
(2, 5)	2.83 ± 1.21	10.94 ± 0.63	0.21 ± 3.05
(4, 5)	2.12 ± 1.12	11.07 ± 0.26	0.09 ± 0.77
(0, 6)	1.04 ± 1.71	09.81 ± 1.07	1.13 ± 5.05
(2, 6)	1.84 ± 1.95	10.45 ± 0.53	0.15 ± 1.91
(4, 6)	2.08 ± 0.81	10.72 ± 0.12	0.19 ± 0.22
(0, -1)	2.17 ± 1.08	32.13 ± 0.37	7.76 ± 1.63
(2, -1)	2.22 ± 1.16	29.60 ± 0.74	7.61 ± 1.99
(4, -1)	2.33 ± 0.63	19.80 ± 0.54	0.44 ± 2.13
(6, -1)	2.33 ± 1.05	17.81 ± 0.41	0.68 ± 0.91
(0, -2)	5.23 ± 2.53	39.28 ± 0.21	8.41 ± 0.81
(2, -2)	1.51 ± 0.83	22.95 ± 0.28	1.51 ± 0.83
(4, -2)	2.32 ± 1.19	09.91 ± 1.88	7.71 ± 0.73
(6, -2)	3.83 ± 2.06	14.41 ± 0.57	1.61 ± 0.22
(0, -3)	2.85 ± 2.11	44.82 ± 0.33	7.21 ± 0.14
(2, -3)	1.36 ± 0.71	36.48 ± 1.04	5.59 ± 0.24
(4, -3)	2.31 ± 0.75	23.24 ± 1.04	0.52 ± 0.36
(6, -3)	2.57 ± 1.07	19.46 ± 0.67	0.13 ± 0.24
(0, -4)	4.49 ± 3.28	51.04 ± 0.32	7.19 ± 0.66

(2, -4)	0.46 ± 0.35	37.91± 2.23	0.46 ± 0.35
(4, -4)	1.67 ± 0.55	30.86 ± 1.31	3.11 ± 1.31
(6, -4)	2.19 ± 0.88	22.89 ± 1.01	1.19 ± 1.33
(0, -5)	6.31 ± 0.24	59.91 ± 1.94	6.31 ± 2.05
(2, -5)	0.61 ± 0.26	43.48 ± 1.31	0.61 ± 0.26
(4, -5)	1.71 ± 0.49	42.33 ± 1.27	3.69 ± 1.41
(0, -6)	-3.01 ± 0.15	19.28 ± 1.39	2.91 ± 0.51
(2, -6)	1.39 ± 0.81	10.32 ± 0.12	7.74 ± 0.22
(4, -6)	1.44 ± 0.38	47.39 ± 1.72	1.41 ± 2.05

APPENDIX F

LIST OF ACHIEVEMENTS

1. **Muhammad Masud Rana,** Debarati Nath, Stephen Pistorius, "Sensitivity Analysis of a Portable Microwave Breast Cancer Detection System," 7th International Conference on Biomedical Engineering and Systems (ICBES'20), Czech Republic.